IEEE Access
Multidisciplinary | Rapid Review | Open Access Journal

Received January 8, 2021, accepted February 22, 2021, date of publication February 26, 2021, date of current version March 10, 2021.

Digital Object Identifier 10.1109/ACCESS.2021.3062764

A Multistage Hybrid Model ICEEMDAN-SE-VMD-RDPG for a Multivariate Solar Irradiance Forecasting

MUHAMMAD SIBTAIN[1], XIANSHAN LI[1], SNOOBER SALEEM[2], QURAT-UL-AIN[3], MUHAMMAD SAQLAIN ASAD[4], TOUSEEF TAHIR[5], AND HALIT APAYDIN[6]

[1]Laboratory for Operation and Control of Cascaded Hydropower Station, China Three Gorges University, Yichang 44302, China
[2]Department of Economics, National University of Modern Languages, Islamabad 44000, Pakistan
[3]Hailey College of Banking and Finance, University of the Punjab, Lahore 54590, Pakistan
[4]National Design and Engineering Solutions, Lahore 54000, Pakistan
[5]Mangla Power Station, Mirpur 10200, Pakistan
[6]Department of Agricultural Engineering, Faculty of Agriculture, Ankara University, 06110 Ankara, Turkey

Corresponding author: Muhammad Sibtain (sibtain92@ctgu.edu.cn)

This work was supported in part by the National Natural Science Foundation of China under Grant 51607105 and in part by the Provincial Natural Science Foundation of HUBEI Province Grant 2016CFA097.

ABSTRACT Accuracy of solar irradiance forecasting is imperative for the effective utilization and integration of solar energy into the power system. To forecast global horizontal irradiance based on a multivariate meteorological data; this study first evaluates five standalone models, including recurrent deterministic policy gradient (RDPG), long short term memory (LSTM) neural network, extreme gradient boosting (XGB), Gaussian process regression (GPR), and support vector regression (SVR). The RDPG model outperforms the standalone counterparts by demonstrating 2.485 W/m^2, 20.591 W/m^2, 18.316 W/m^2, and 23.176 W/m^2 reductions in RMSE compared to the LSTM, XGB, GPR, and SVR models. Afterward, the performance of the RDPG model is further enhanced, by developing two-stage hybrid models, including improved complete ensemble empirical mode decomposition with additive noise-RDPG (ICEEMDAN-RDPG) and variational mode decomposition-RDPG (VMD-RDPG). The subsequent construction of the hybrid model ICEEMDAN-SE-VMD-RDPG (ISVR) results in the further improvement of the two-stage hybrid models. The ISVR surpasses all the established models including VMD-RDPG, ICEEMDAN-RDPG, RDPG, LSTM, XGB, GPR, and SVR by displaying 18.401 W/m^2, 13.908 W/m^2, 33.223 W/m^2, 53.111 W/m^2, 67.704 W/m^2, 67.502 W/m^2 and 69.943 W/m^2, respectively, decrease in RMSE. The overall results are enlightening and reveal the extension feasibility of the IVSR model for the other forecasting tasks, e.g., renewable energy integration and electrical load forecasting.

INDEX TERMS Solar irradiance forecasting, decomposition techniques, sample entropy, correlation, deep reinforcement learning.

NOMENCLATURE

ADN	Active Distribution Network
ANN	Artificial Neural Network
AP	Air Pressure
AT	Air Temperature
DDM	Data-Driven Model
DDPG	Deep Deterministic Policy Gradient
DL	Deep Learning
DLM	Deep Learning Model
DPG	Deterministic Policy Gradient
d_r	Willmott's refined index of agreement
ML	Machine Learning
MLM	Machine Learning Model
NSE	Nash-Sutcliffe coefficient of Efficiency
PACF	Partial Autocorrelation Function
RDPG	Recurrent Deterministic Policy Gradient
RER	Renewable Energy Resource
RH	Relative Humidity
RL	Reinforcement Learning
RMSE	Root Mean Square Error
RNN	Recurrent Neural Network

The associate editor coordinating the review of this manuscript and approving it for publication was Ikramullah Lali.

This work is licensed under a Creative Commons Attribution 4.0 License. For more information, see https://creativecommons.org/licenses/by/4.0/

DRLM	DRL Model
EMD	Empirical mode decomposition
GHI	Global Horizontal Irradiance
GHI_t	Observed GHI
$\hat{GHI}_t$	Forecasted GHI
GPR	Gaussian Process Regression
HIF1-HIF10, R	Decomposed components for RH series by ICEEMDAN
HVF1-HVF4	Decomposed components for HIF1 mode through VMD
ICEEMDAN	Improved Complete Ensemble Empirical Mode Decomposition With Additive Noise
ISVR	ICEEMDAN-SE-VMD-RDPG
LSTM	Long Short Term Memory
MAE	Mean Absolute Error
MAPE	Mean Absolute Percentage Error
SE	Sample Entropy
sMAPE	Symmetric Mean Absolute Percentage Error
SVR	Support Vector Regression
TIF1-TIF9, R	Decomposed components for AT series by ICEEMDAN
TVF1-TVF4	Decomposed components for TIF1 mode through VMD
VMD	Variational Mode Decomposition
WD	Wind Direction
WIF1-WIF10, R	Decomposed components for WSG series by ICEEMDAN
WS	Wind Speed
WSG	Wind Speed of Gust
WVF1-WVF6	Decomposed components for WIF2 mode through VMD
XGB	Extreme Gradient Boosting

I. INTRODUCTION

The adverse impact of fossil fuels, including the exhaustible nature, environmental concerns, and high costs, are shifting the energy paradigm towards the increasing utilization of RERs. RERs, including solar, wind, hydro, geothermal, and biomass, are present in abundance in Pakistan [1]. Pakistan receives nearly 5-7 kWh/m^2/day of solar irradiation, which is promising for solar energy generation. The northeastern region of Sind province and the southwestern part of Balochistan province are immensely feasible for exploiting solar energy in the country [2]. The average sunshine hours are between 8-10 h/day and 1500-3000 h (300 days) per year [3].

Solar energy is considered one of the cleanest RER with the least harmful effect on the environment [4]. However, the intermittent nature of solar irradiance poses a challenge in harnessing solar power. Therefore, forecasting techniques are necessary to ensure sustainable and reliable solar power generation [5]. Forecasting can also be applied to control the virtual inertia of photovoltaic systems and to regulate the frequency of islanded microgrid [6]. A surfeit of studies applied ML based DDMs to forecast solar irradiance [7], which included the classical and hybrid approaches [8]. MLMs, including SVR [9], ANN [10]–[12], random forest, and gradient boosted regression [9], were commonly implemented in classical approaches [8]. Li *et al.* [13] tested SVR and hidden markov model through experimental evaluations and accuracy metrics, which verified the applicability of both models for irradiance forecasting. The GHI forecasting was improved by employing the satellite data to ANN. The proposed ANN model revealed better results than the smart persistence model and the climatological mean model in terms of RMSE, MAE, and the skill metric [14]. Benali *et al.* [15] developed three models, including ANN, random forest, and smart persistence, to forecast hourly irradiations. The random forest model showed the best results for MAE, RMSE, normalized MAE, and normalized RMSE [15].

Support vector machine was proposed by Vapnik [16], is a MLM for pattern recognition and data analysis, and has also widespread applicability for solar radiation forecasting [17]. Support vector machine employs kernel functions that convert the original data into a higher-dimensional feature space. In this way, the distance between the nearest point of each class and the hyper-plane is maximized. The radial basis function kernel has a better performance compared to the other kernels for solar radiation forecasting tasks [18]. Support vector machine can be implemented as SVR for regression problems. The solar radiation forecasting tasks were also implemented by employing models including XGB [19], [20] and GPR [21], [22]. The popularity of the GPR model has increased over recent years. As a non-parametric model, GPR performs the task of regression by utilizing the prior of Gaussian process [23]. The GPR adopts the kernel function based on Bayes linear regression, which increases its ability to deal with intricate and nonlinear problems [24]. XGB model is based on random forest and gradient boosting decision tree models and was developed by Chen and Guestrin [25]. To develop a strong learner by the boosting process, the forecasts of weak learners are combined by employing the additive training approaches. The final forecasting result is based on summing the forecast of each learner [18]. DLMs comprising LSTM neural network and gated recurrent unit neural network also presented superior results in forecasting solar irradiance, compared to the other MLMs [26]–[28]. Qing and Niu [26] utilized the LSTM model for hourly day-ahead forecasting of solar irradiance. The LSTM based model outperformed the other comparison models, including the backpropagation neural network, linear least square regression, and persistence algorithm, in terms of the RMSE metric. Gao *et al.* [27] verified the superiority of the gated recurrent unit over backpropagation neural network, RNN, and LSTM models in terms of RMSE and forecast skill metrics, to forecast day-ahead solar irradiance. The development of the hybrid DL models, based on an integration of DL with an attention mechanism, further enhanced the performance of the standalone DL models [29], [30]. The DLMs are viable replacements of the conventional

DDMs [31], [32]. The multiple processing layers in DL allow better management of the input data due to their deeper structures [33]. RL is a type of evolutionary process that involves the interface among individuals and the surrounding [34].

With the rapid advancement in the field of DRL, the DRLMs are also becoming popular in the field of forecasting. The RL agent implements learning in a complex and ambiguous environment to realize an objective. The action performed determines the reward of the agent gained by the environment. The machine is regarded as an agent, whereas the surroundings play the role of the environment [35].

DRLMs integrate DL techniques with RL methods to handle intricate problems with large state and action spaces [33]. The DRLMs proficiently resolve a wide range of complex decision-making problems, which were previously beyond the expertise of ML. The DRLMs apply to the fields, including robotics, energy management, computer vision, finance, natural language processing and, so on [35]. The DRLMs also find successful implementation to achieve the goal of forecasting. Elavarasan and Vincent [35] employed a hybrid combination of RNN and Q-learning algorithm to forecast crop yield for farming applications. RNN was utilized as a DLM, whereas; Q-learning algorithm served the purpose of the RL algorithm. The proposed model excelled at the other DDMs in the training and testing periods [35]. Park *et al.* [36] applied RL based on Deep Q-Network to select a similar day in the short-term load forecasting by deploying a backpropagation neural network. The developed model transcended the LSTM model load forecasting algorithm [36]. The integration of frequency domain clustering of data, with expected state-action-reward-state-action algorithm, was implemented for the effective operation of the energy storage system. The proposed approach effectively handled the uncertainty of wind power forecasting compared to the Q-learning algorithm [37]. Space discretization is a requirement in pure Q-learning, and an increase in scenario numbers results in an exponential growth of computational cost [38]. State-action-reward-state-action algorithm also has limitations for continuous domain applications; since it is feasible for discrete action and state space [39]. A large number of complex control problems involving continuous action spaces; can be satisfactorily solved by applying an off-policy gradient algorithm, namely, the DPG [40]. The actor-critic DPG algorithm obtains estimated action-value gradients to update policy by employing a learned estimation of the action-value function [41]. The DDPG algorithm; was proposed by introducing deep neural networks in the DPG algorithm for an effective learning process. DDPG learns Q-function by using the off-policy data and the Bellman equation, while the policy learning occurs by employing the Q-function. Due to the off-policy training of the network with replay buffer samples, the learning process of value function occurs robustly and stably. This superior learning enables the successful implementation of DDPG in a variety of observable problems [40]. Liu *et al.* [33] applied the DDPG model to forecast the energy consumption by the heating, ventilation, and air-conditioning system. The analysis revealed better forecasting outcomes of the DDPG model compared to the SVR and backpropagation neural network [33]. The present study deals with GHI forecasting, which considers uncertain environmental variables. Therefore, the DDPG is not suitable enough in the present study in estimating the action-value function due to limitations of the feedforward neural network of DDPG in capturing the complex nonlinearity. The above literature also highlights the shortcomings of the ML and DRL based ML models for efficient forecasting, considering the uncertainty of the environmental variables. To deal with the situation and for reliable GHI forecasting, this study employs RDPG, which is a RNN variant of DPG [41]. The RDPG algorithm employing the LSTM network presented a reliable performance in solving complex tasks compared to the other DRL counterparts [41]. Therefore, we employ LSTM based RNN in RDPG that offers superior ability to extract data from the time series with suitability for learning long-term dependencies of the time series and preserving information about the past [42].

Despite the applicability of the standalone DDMs for solar irradiance forecasting and similar applications, these models have limitations in capturing the deterministic features of the historical data. These constraints of the individual DDMs have resulted in the development of hybrid models, which aim to augment the model performances by extracting all the relevant features from the input data [8]. One of the approaches to construct hybrid models involved the integration of signal decomposition techniques with the MLMs [43]–[45]. Liu *et al.* [34] accomplished the task of short-term wind speed forecasting by developing a hybrid DRL model, which integrated empirical wavelet transform with DLMs based on the Q-learning algorithm. The established ensemble models yielded better results than the other established hybrid and standalone models [34]. The ICEEMDAN is the latest version of EMD based techniques with better decomposition properties than its predecessors. The hybrid forecasting models, with a single decomposition stage, can be upgraded further by employing VMD as a second decomposition stage. In the dual decomposition stage hybrid models, VMD decomposed the high-frequency components generated in the first decomposition stage [46], [47].

The literature investigation highlights the application prospects and the robust implementation of DRLMs in various fields, including forecasting and ensemble learning. Therefore, considering the DL viability for time series forecasting, the practicability of ensemble learning models, and the robust learning performance exhibited by the integration of decomposition techniques, DLMs, and RL, a hybrid model ISVR is proposed in this study to forecast GHI. The ISVR model is structured; on an ensemble of ICEEMDAN, SE, VMD, and RDPG. ICEEMDAN is applied to concurrently decompose the time-series signals into respective modes and a residual component. The component with the highest value of SE is decomposed, by VMD, in the second decomposition stage. PACF analysis is employed, to the decomposed

components obtained, through the two-stage decomposition. RDPG is applied, in the final step, of the forecasting process. Seven other models, including ICEEMDAN-RDPG, VMD-RDPG, LSTM, XGB, GPR, and SVR, are also developed for a relative analysis.

The rest of the paper is structured as follows: Section II presents a review of ICEEMDAN, SE, VMD, and RDPG techniques. Section III provides a comprehensive description of the proposed ISVR model, data preparation methodology, and the statistical indices. Section IV compares and discusses the results of the proposed model with the benchmark models and presents directions for future study. Finally, Section V concludes the study.

II. MATERIALS AND METHODS

A. ICEEMDAN

ICEEMDAN is an advanced version of EMD based techniques, which resolves the problems of frequency aliasing and spurious modes as suffered by its predecessors. The addition of white noise realizes the continuity of frequency among adjacent scales with consequent fading of the effect of frequency mixing. Following equations summarize the main steps of the ICEEMDAN [48]:

(i) Determine the realizations of local means by EMD as mentioned below:

$$s^i = s + \beta_0 E_1\left(w^i\right) \tag{1}$$

where i is the added noise numeral, s is the original signal, s^i indicates the signal for decomposition, w^i denotes the white noise and $E_1(w^i)$ represents first component of white noise.

(ii) Subsequently, the first residue (R_1) can be determined as:

$$R_1 = \left\langle M\left(s^i\right)\right\rangle \tag{2}$$

where $M(\cdot)$ symbolizes the local mean to accomplish the sifting point of IMF.

(iii) The first mode can be calculated, at the first stage, after the decomposition of N signals as:

$$IMF_1 = s - R_1 \tag{3}$$

(iv) The succeeding steps determine the second residue and mode as:

$$R_2 = \left\langle M\left(R_1 + \beta_1 E_2\left(w^i\right)\right)\right\rangle \tag{4}$$

$$IMF_2 = R_1 - R_2 \tag{5}$$

(v) Compute the *kth* residue and mode as:

$$R_k = \left\langle M\left(R_{k-1} + \beta_{k-1} E_k\left(w^i\right)\right)\right\rangle \tag{6}$$

$$IMF_k = R_{k-1} - R_k \tag{7}$$

(vi) Repeat (4) for the subsequent k stages.

B. VARIATIONAL MODE DECOMPOSITION

VMD is a fully adaptive and intrinsic model that appropriately balances the error between modes by an adaptive determination of relevant bands with a concurrent estimation of the corresponding modes. VMD overcomes the limitations of existing decomposition techniques like lack of mathematical theory as faced by EMD, the restriction of backward error improvement due to recursive sifting in most methods, and appropriate noise handling ability [49]. The constrained variational problem can be given below

$$\begin{aligned} &f(t) \\ &= \min_{\{u_k\},\{\omega_k\}}\left\{\sum_k \left\|\partial_k\left[u_k(t) * \left(\frac{\delta(t)\pi t + j}{\pi t}\right)\right] e^{-j\omega_k t}\right\|_2^2\right\} \\ &\quad s.t. \sum_k u_k \end{aligned} \tag{8}$$

where $\{u_k\}$ and $\{\omega_k\}$ denote modal component and centre frequencies, respectively. The introduction of the quadratic penalty and Lagrangian multipliers transform the above-constrained problem into the subsequent unconstrained form:

$$\begin{aligned} &L(\{u_k\},\{\omega_k\},\lambda) \\ &= \alpha\left\{\sum_k \left\|\partial_t\left[u_k(t) * \left(\frac{\delta_t \pi t + j}{\pi t}\right)\right] e^{-j\omega t}\right\|_2^2\right\} \\ &\quad + \left\|f(t) - \sum_k u(t)\right\|_2^2 + \left\langle \lambda(t), f(t) - \sum_k u_k(t)\right\rangle \end{aligned} \tag{9}$$

The integration of the quadratic penalty and Lagrangian multipliers provides the benefits of outstanding convergence abilities of the quadratic penalty and firm implementation of the constraint by the Lagrangian multiplier. The solution of equation (9) is possible by applying the alternative direction method of multipliers. The two steps of equation (9) can be given under:

(i) u_k minimization

$$\widehat{u}_k^{n+1}(\omega) = \frac{\widehat{f}(\omega) - \sum_{i\neq k}\widehat{u}(\omega) + \frac{\widehat{\lambda}(\omega)}{2}}{1 + 2\alpha(\omega - \omega_k)^2} \tag{10}$$

(ii) ω_k minimization

$$\omega_k^{n+1} = \frac{\int_0^\infty \omega\left|\widehat{u}_k(\omega)\right|^2 d\omega}{\int_0^\infty \left|\widehat{u}_k(\omega)\right|^2 d\omega} \tag{11}$$

where n represents the iteration number, while the Fourier transform of $\lambda(\omega), u_k^{n+1}, f(\omega), u_i(\omega)$ are denoted by $\widehat{\lambda}(\omega), \widehat{u}_k^{n+1}, \widehat{f}(\omega), \widehat{u}_i(\omega)$, respectively. The comprehensive process of VMD technique is provided in [49].

C. SAMPLE ENTROPY

SE represents the complexity of a finite interval time series by calculating the probability of obtaining new patterns from

the original time series. Higher SE is exhibited by less foreseeable time series; whereas, the time series with regular patterns reveals a smaller SE value [50]. The SE process can be explained by the following steps [51]:

(i) The time series with N points as the original data can be given as

$$s(1), s(2), s(3), \ldots, s(N) \tag{12}$$

(ii) The m dimension reconstruction of the above series is:

$$X(1), X(2), X(3), \ldots, X(N-m+1) \tag{13}$$

where,

$$S_m(i) = [s(i), s(i+1), s(i+2), \ldots, s(i+m-1)] \tag{14}$$

(iii) The distance among $S_m(j)$ ($d[S_m(i), S_m(j)]$) and $S_i(i)$ is:

$$d[X_m(i), X_m(j)] = \max_{k=0,m-1}(|u(i+k) - u(j+k)|) \tag{15}$$

(iv) The mean value of vectors can be obtained as

$$B^m(r) = \frac{1}{N-m+1}\sum_{i=1}^{N-m+1} B_i^m(r) \tag{16}$$

(v) Repeat (ii)-(iv) to obtain $B^{m+1}(r)$ after the increment of dimension m by 1 to express the SE as:

$$SE(m, r) = \lim_{N\to\infty}\left[-\ln\frac{B^{m+1}(r)}{B^m(r)}\right] \tag{17}$$

(vi) The value of N is generally finite, therefore, Equation (17) can also be written as:

$$SE(m, r, N) = \lim_{N\to\infty}\left[-\ln\frac{B^{m+1}(r)}{B^m(r)}\right] \tag{18}$$

where m denotes dimensions and r indicates the conditional threshold.

D. RDPG

RDPG is an RNN-based DRL model that employs a combination of RNN and DPG. RDPG is an actor-critic framework and deploys an off-policy gradient. The action is performed by the actor; whereas, the critic network is employed to assess the quality of action. The LSTM can also be deployed, as RNN, for the actor-critic architecture [41]. The critic network employing LSTM produced more robust forecasting than the DDPG model owing to its ability for the collection of observations over time [52]. The RNN can be utilized for forecasting the partially observed environment due to the existence of a high correlation among the sequence of observations. The hidden state, which also acts as a memory, can capture information regarding its prior actions and observations that is significant for better decision making. The flow of information inside every memory block is controlled by the input, forget, and output gates of LSTM [53], [54]. The basic structure of LSTM is explained below:

$$\text{Input gate } i_t = \sigma(U_i W_t + V_i h_{t-1} + b_i) \tag{19}$$

$$\text{Output gate } o_t = \sigma(U_o W_t + V_o h_{t-1} + b_o) \tag{20}$$

$$\text{Forget gate } f_t = \sigma\left(U_f W_t + V_f h_{t-1} + b_f\right) \tag{21}$$

$$\text{Hidden state } h_t = \tanh(C_{t-1}) * o_t \tag{22}$$

$$\text{Cell input } \tilde{C}_t = \tanh(U_c W_t + V_c h_{t-1} + b_c) \tag{23}$$

$$\text{Cell state } C_t = C_{t-1} * f_t + \tilde{C}_t * i_{t-1} \tag{24}$$

wher W_t is input at time step t, h_{t-1} represents hidden states, σ and tanh shows sigmoidal and hyperbolic tangent function, respectively, the network weights are U_s and V_s, and b_s are bias vectors. References [41, 52] provide a detailed description and implementation of the DRL based RDPG approach.

E. STATISTICAL MEASURES

The commonly employed statistical measures for solar resource forecasting applications include RMSE, MAE and MAPE [29], [30], [55]. The accurate forecasting of solar irradiance is an intricate process due to the stochastic and intermittent nature of the solar irradiance [28], [56]. The solar irradiance is only present during the daytime, whereas it has a very low or zero value during the night. Because of the zero values of GHI, MAPE is not suitable for the present study due to limitations of extreme values and asymmetry. However, sMAPE avoids all problems as suffered by MAPE [57], [58]. Moreover, sMAPE is also extensively employed statistical measure for solar resource forecasting tasks [59]. The NSE [60] and d_r [61] statistical measures also provide a meaningful comparison to assess the models performance. Hence, this study employs RMSE, MAE, sMAPE, NSE, and $_{dr}$ to evaluate the performance of the proposed and the benchmark models. These statistical measures can be defined by the following equations:

$$RMSE = \sqrt{\frac{1}{n}\sum_{t=1}^{n}\left(GHI_t - \hat{GHI}_t\right)^2} \tag{25}$$

$$MAE = \frac{1}{n}\sum_{t=1}^{n}\left|GHI_t - \hat{GHI}_t\right| \tag{26}$$

$$sMAPE = \frac{2}{n}\sum_{t=1}^{n}\frac{\left|GHI_t - \hat{GHI}_t\right|}{\left(|GHI_t| + \left|\hat{GHI}_t\right|\right)} \times 100 \tag{27}$$

$$NSE = 1 - \frac{\sum_{t=1}^{n}\left(GHI_t - \hat{GHI}_t\right)^2}{\sum_{t=1}^{n}\left(GHI_t - \overline{GHI_t}\right)^2} \tag{28}$$

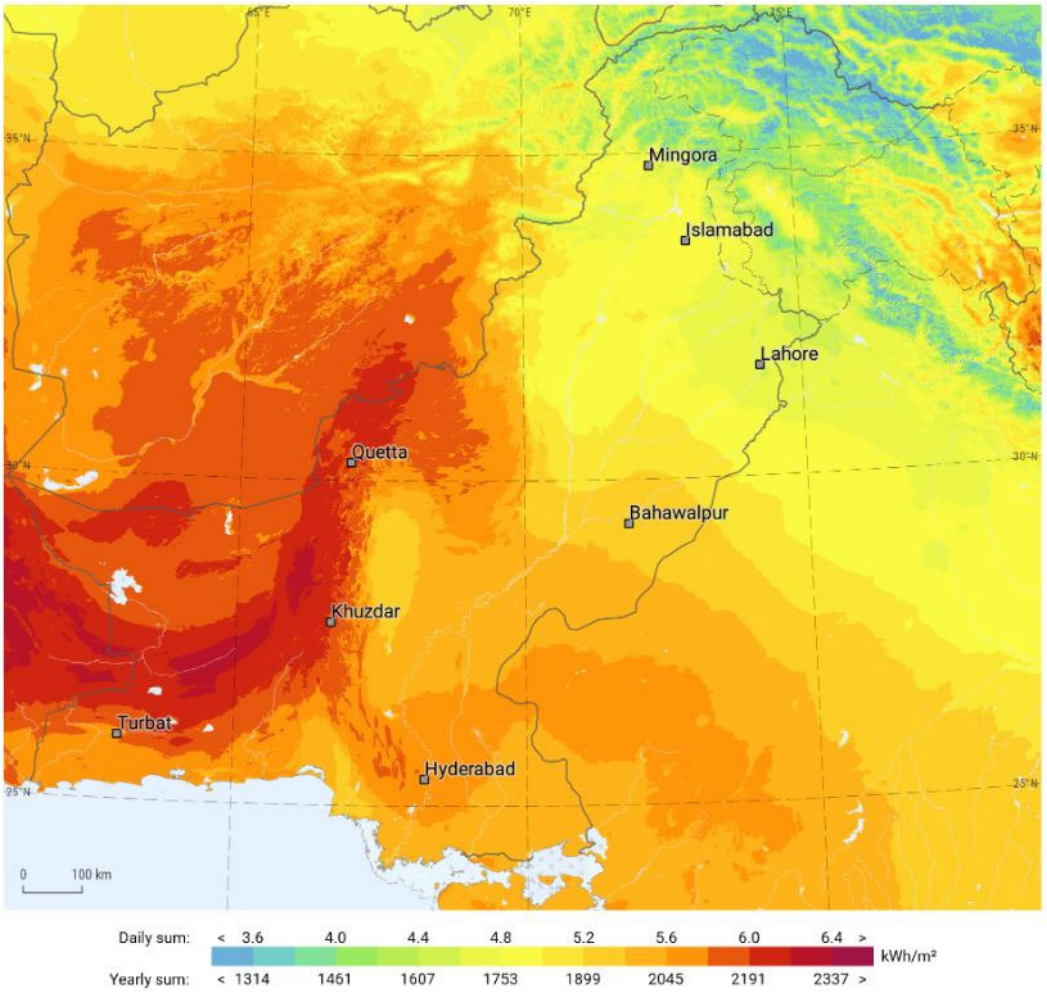


FIGURE 1. Global horizontal irradiation map of Pakistan.

$$d_r = \begin{cases} 1 - \dfrac{\sum_{t=1}^{n} \left| \hat{GHI}_t - GHI_t \right|}{c \sum_{t=1}^{n} \left| GHI_t - \overline{GHI_t} \right|} \\ when \sum_{t=1}^{n} \left| \hat{GHI}_t - GHI_t \right| \\ \leq c \sum_{t=1}^{n} \left| GHI_t - \overline{GHI_t} \right| \\ \dfrac{c \sum_{t=1}^{n} \left| GHI_t - \overline{GHI_t} \right|}{\sum_{t=1}^{n} \left| \hat{GHI}_t - GHI_t \right|} - 1 \\ when \sum_{t=1}^{n} \left| \hat{GHI}_t - GHI_t \right| \\ > c \sum_{t=1}^{n} \left| GHI_t - \overline{GHI_t} \right| \end{cases} \tag{29}$$

In Equations (25)-(29), GHI_t, $\hat{GHI}_t$ and $\overline{GHI_t}$ represent the observed, forecasted and mean GHI, respectively. The factor c has a value of 2 and n depicts the number of observations.

III. THE PROPOSED METHODOLOGY

A. STUDY AREA

The present study considers the Khuzdar district of Balochistan province, Pakistan, for GHI forecasting, due to the presence of abundant solar resource potential [62]. The Khuzdar district is located in the southern region of Balochistan. Fig. 1 illustrates the location of the Khuzdar district in the global horizontal irradiation map of Pakistan [63].

B. DATA DESCRIPTION AND INPUT DATA PREPARATION

The data of AT, AP, RH, WS, WSG, and WD is considered in this study to forecast one step ahead GHI. The original data is available with a resolution of 10 minutes [64]. The data of the first week of January-2016, April-2016, July-2016,

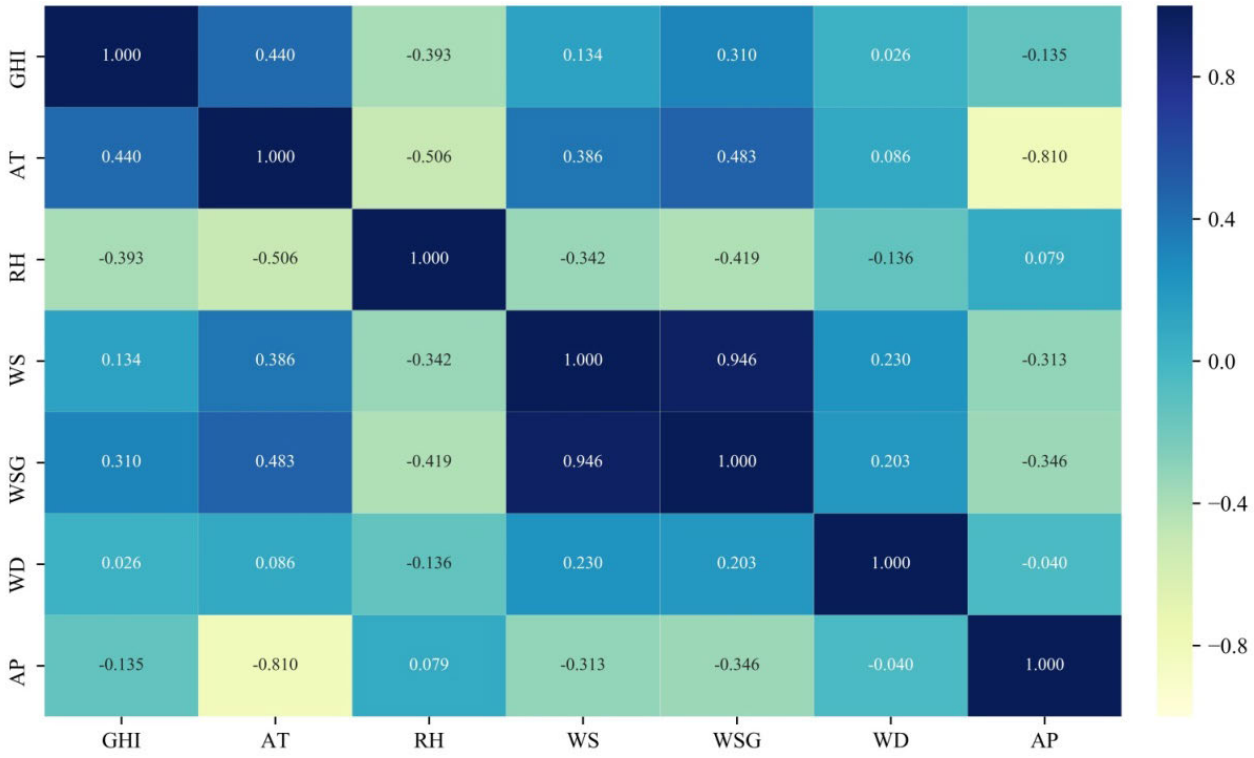


FIGURE 2. Heatmap showing the correlation of variables.

and October-2016, which corresponds to the winter,spring, summer, and autumn seasons, is taken in the present study. The data is further arranged such that the data of the first six days from a week for all these four months are taken together; whereas, the remaining data that represent the seventh day is placed one after another. For a clear understanding, the data of the first six days of January-2016, April-2016, July-2016, and October-2016 are placed together, followed by the seventh day weekly data in the same sequence. This data arrangement aims to divide the seasonal data into an equal amount for a better analysis of the data. After the arrangement of data, the overall sample size obtained for each of the individuals AT, RH, WS, WSG, WD, AP, and GHI time series is 4032 samples. The hardware platform for the present study is a desktop version of Intel core i9-9900KS processor, with a base frequency of 4GHz, 32GB of DDR4 RAM, and NVIDIA GeForce RTX 2080Ti GPU, with 11GB of GDDR6 RAM. The decomposition-based models (ICEEMDAN and VMD), and SE, are implemented in MATLAB 9.4 (R2018a) programming platform developed by MathWorks in a Windows 10, 64-bit operating system. Moreover, the correlation analysis and the PACF analysi; are executed in Python 3.6.9 programming language. Furthermore, the development of all MLMs is also carried out in Python 3.6.9, by utilizing modules including Google Tensorflow 1.10.0 [65], Keras 2.1.2 [66], Pandas 0.24.0 [67], Scikit-learn 0.21.3 [68], Numpy 1.15.4 [69], Matplotlib 3.1.2 [70] and Seaborn 0.9.0 [71]. The Python programming language is implemented in the Community Edition 2019.2.3 of the PyCharm integrated development environment developed by JetBrains.

The correlation analysis is executed as shown in Fig. 2, to select inputs with a significant correlation with the observed GHI data. The variables having correlation values greater than 0.2 are usually considered significant [27], [72]. Only the three variables, including AT, RH, and WSG, show a significant correlation with the GHI. AT and RH variables show a positive correlation, whereas the WSG variable shows a negative correlation with the GHI variable. The correlation values of WS, WD, and AP are not significan; therefore, these are discarded in the further forecasting analysis.

Fig. 3 demonstrates the relationships between two variables and the distribution of individual variables through a pairplot for AT, RH, WSG, and GHI. The portion of the plot on the upper and lower sides of the diagonal depicts the relationship between the two variables. Furthermore, the diagonal histograms show the distribution of the individual variable. For example, the right-most plot in the first row highlights the plot of GHI versus WSG.

C. THE HYBRID FORECASTING MODEL

The framework of the proposed ISVR model is explained in Fig. 4. Moreover, the systematic sequence of the main steps involved in establishing the ISVR model is summarized below:

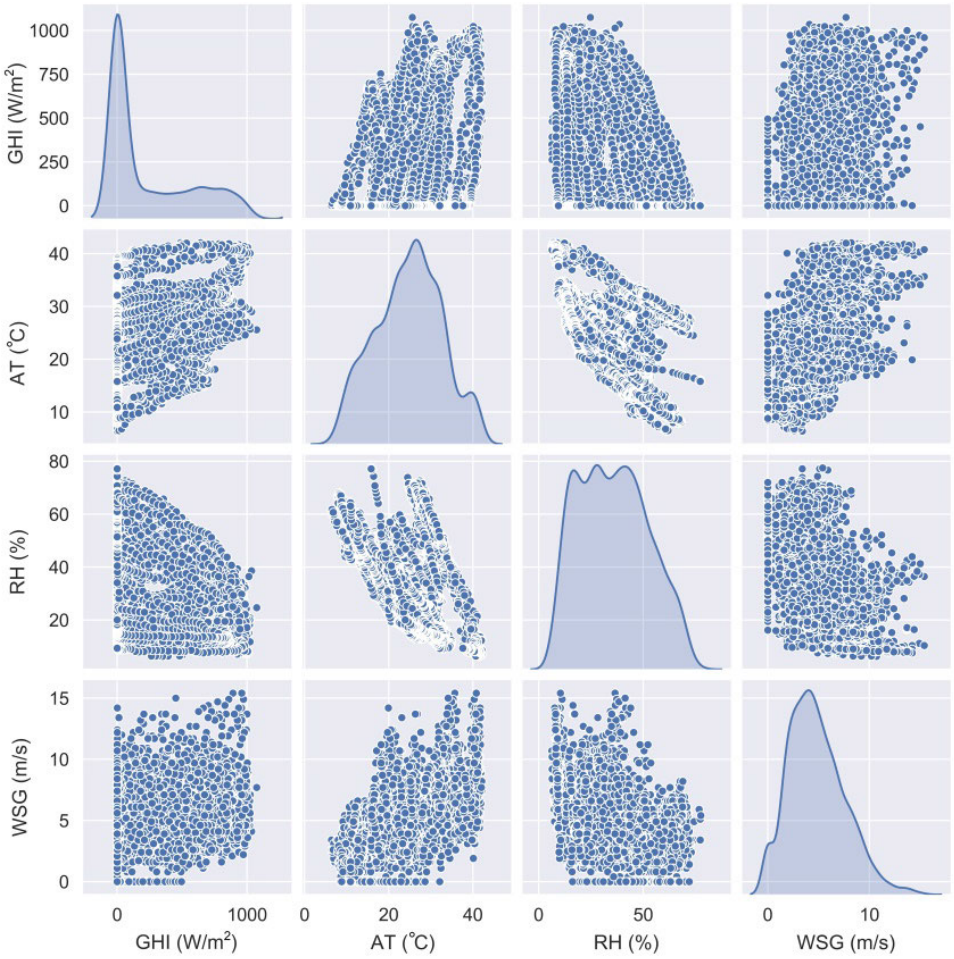


FIGURE 3. Pairplot to illustrate the relationship and the distribution of data.

Step 1: The correlation analysis is performed to select variables from the available data having a significant correlation with the GHI variable.

Step 2: ICEEMDAN is employed to decompose the selected time series of Step 1 into respective modes.

Step 3: SE is applied to determine the mode with the highest entropy value.

Step 4: The secondary decomposition of the modes with the highest value of SE is carried out through VMD.

Step 5: The extraction of input variables for the development of hybrid models is carried out by applying the PACF analysis to the decomposed components obtained through Step 2 and Step 4. Whereas; PACF analysis is deployed to the variables obtained in Step 1 for the establishment of the standalone models.

Step 6: The selected inputs of Step 5 are applied to the ML models to construct the forecasting framework. The reconstruction of the forecasted results accomplishes the forecasting task.

Step 7: The performance of the ISVG model is analyzed and compared with the benchmark models to draw the conclusions.

IV. FORECASTING MODELS DEVELOPMENT

A. DECOMPOSITION BY ICEEMDAN

To forecast the one-step-ahead GHI, the time series of AT, WSG, and RH, are decomposed by ICEEMDAN into ten modes (TIF1-TIF9, R), eleven modes (WIF1-WIF10, R), and eleven modes (HIF1-HIF10, R), respectively, as shown in Fig. 5. The decomposition process proceeds by considering the value of noise amplitude as 0.2, the number of realizations as 100, and the same SNR for all decomposition modes. The detailed parameters setting of the ICEEMDAN process is available in [48]. The ICEEMDAN processing is employed to lessen the non-linear and non-stationary features of AT, WSG, and RH time series by decomposition it into several modes. The modes generated by ICEEMDAN processing; are arranged in a sequence, with an increasing wavelength

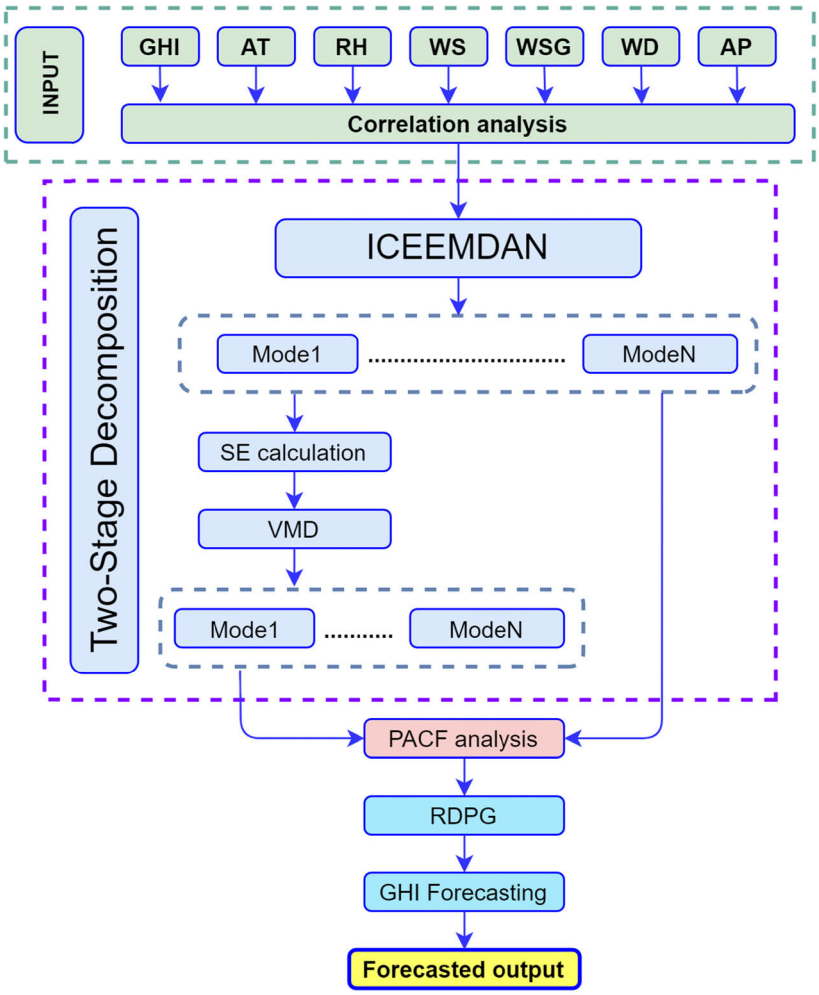


FIGURE 4. The ISVR model main steps flowchart.

and a decreasing frequency. Consequently, TIF1, WIF1, and HIF1 modal components have evidenced the highest frequency with the lowest wavelength; whereas, the R (residual) components have revealed the highest wavelength with the lowest frequency.

B. SAMPLE ENTROPY CALCULATION

The SE values for each mode obtained through ICEEMDAN for AT, WSG, and RH time series, are calculated by determining the model with the highest value of SE. The highest values of SE are revealed by TIF1, WIF2, and HIF1 modes, for the AT, WSG, and RH time series, respectively, as demonstrated by Table 1. For SE calculation, the value of the number of dimensions (m) is taken as 2, whereas the conditional threshold (r) is 0.2 times the standard deviation of the data series under consideration.

C. DECOMPOSITION BY VMD

The secondary decomposition of the modes with the highest values of SE is carried by employing VMD. As illustrated in Fig. 6, four modes (TVF1-TVF4), six modes (WVF1-WVF6), and four modes (HVF1-HVF4) are obtained, by the decomposition of TIF1, WIF2, and HIF1 components, respectively, after employing the VMD technique. Unlike ICEEMDAN and the other EMD based decomposition techniques, the VMD offers an adaptive decomposition of the signal without the generation of residual modes. The secondary decomposition of the components with the highest SE value by VMD further resolves the low-frequency patterns for more accurate forecasting results. The parameters setting for VMD include bandwidth constraint value of 1000 and a shutoff Lagrangian multiplie ($\tau = 0$) r. The number of modes (K) for TIF1, WIF2, HIF1 is 4, 6, 4, respectively, as determined through the center frequency method. The process involves no DC part imposed, uniform initialization of center frequencies, and the tolerance level (ε) of $1E^{-7}$. Reference [49] provides a detailed description of theparameters setting for the VMD process.

D. PACF ANALYSIS AND DATA SELECTION

Feature extraction for setting up the standalone, and the hybrid models, are based on the PACF analysis. The determination of the input matrix is necessary before sending

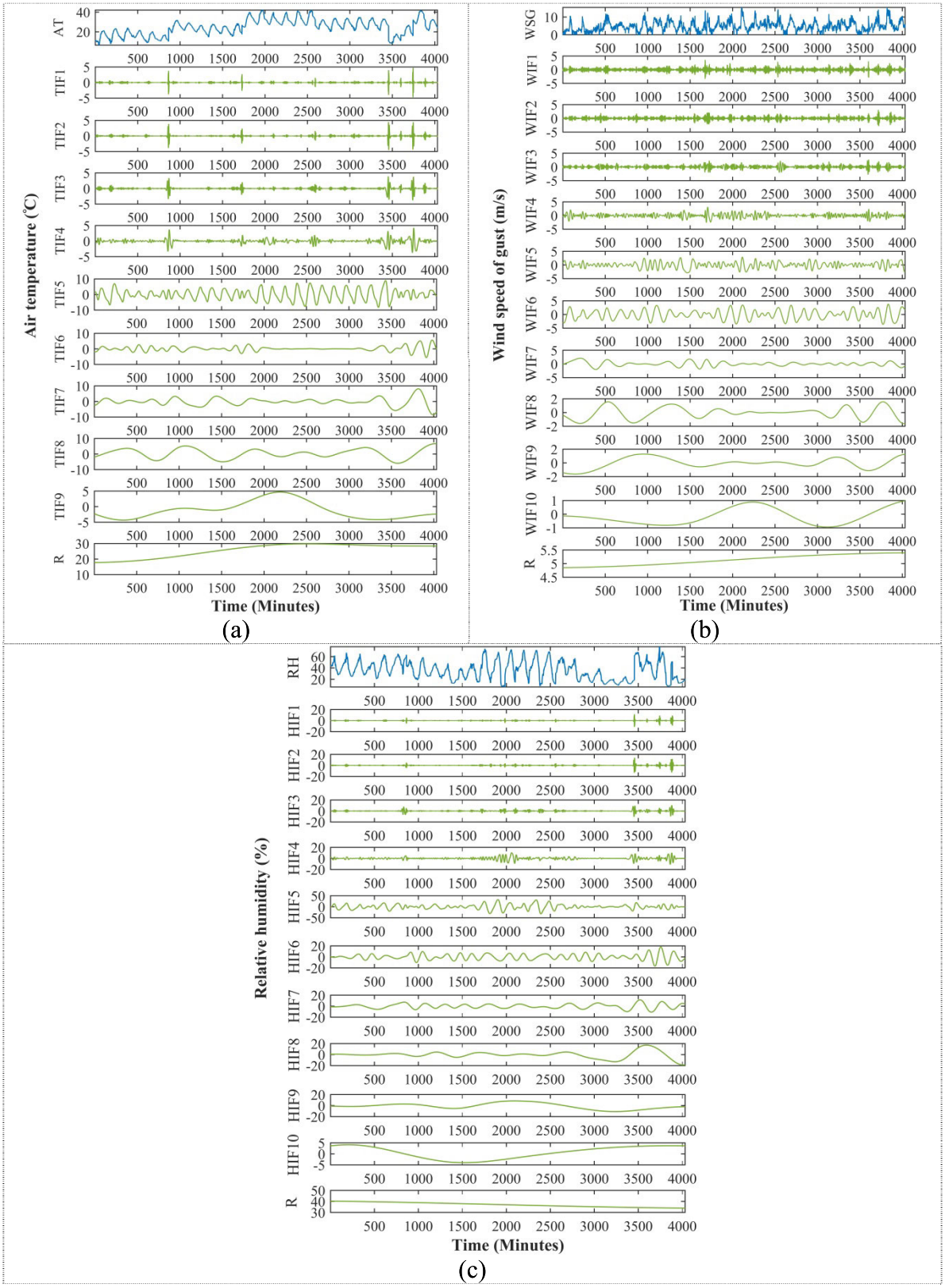


FIGURE 5. The decompositions of the three-time series by ICEEMDAN. (a) Air temperature (AT), (b) Wind speed of gust (WSG), (c) Relative humidity (RH).

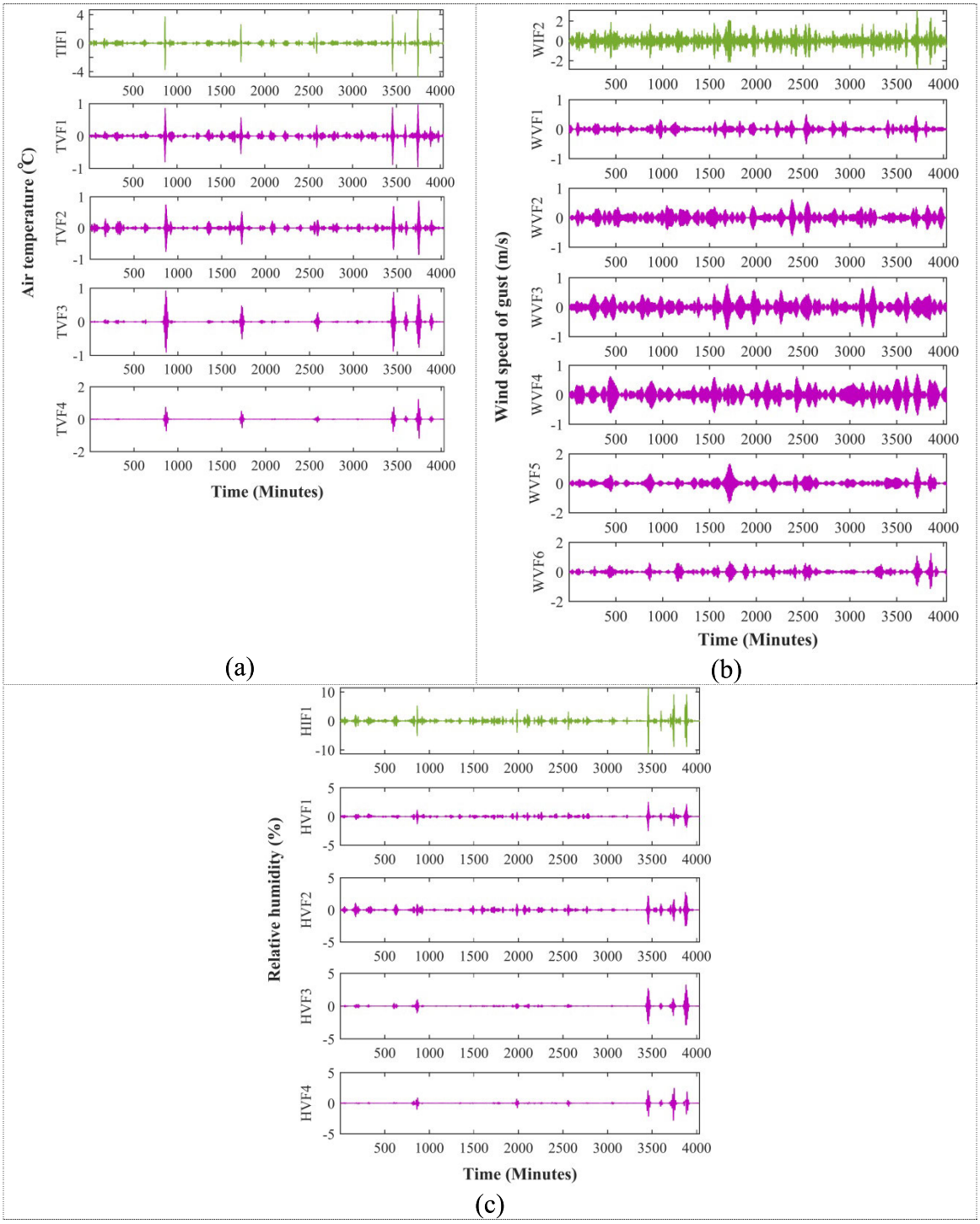


FIGURE 6. The secondary decompositions of the modes with the highest sample entropy by VMD. (a) Air temperature (TIF1), (b) Wind speed of gust (WIF2), (c) Relative humidity (HIF1).

data into the developed models since the excellence of forecasting results is dependent on the input variables. PACF analysis is applied to the decomposed components, obtained through ICEEMDAN and the secondary decomposition by VMD, to calculate the PACF values for the selection of significant and appropriate variables for forecasting models. The same scheme of input selection is deployed, for all the developed models, to guarantee a valid and rational assessment. For brevity, only the results of PACF analysis for the establishment of the ISVR model are shown

TABLE 1. Sample entropy calculation for the AT, WSG, and RH time series.

Mode	Variable		
	AT	RH	WSG
Mode1	**1.8289**	**0.9383**	2.0228
Mode2	1.4719	0.5870	**2.3068**
Mode3	1.0055	0.3612	1.7987
Mode4	0.4235	0.1329	0.9573
Mode5	0.0403	0.0057	0.2736
Mode6	0.0400	0.0176	0.0815
Mode7	0.0130	0.0127	0.0785
Mode8	0.0074	0.0020	0.0323
Mode9	0.0021	0.0014	0.0163
Residual/Mode10	0.0001	0.0013	0.0124
Residual	-	0.0001	0.0005

here in Fig. 7 (A), (B), (C). The components having significant values of correlation, with the original decomposed modal component, are selected as one set of inputs to the MLMs.

For the ISVR model, forty-six components have shown the PACF values greater than 0.2, which are selected as inputs to the MLMs. The number of components selected based on PACF analysis of the AT, WSG, and RH time series decomposed modal components by VMD are twenty-two for the VMD-RDPG model. Similarly, the PACF analysis of the decomposition of AT, WSG, and RH time series by ICEEMDAN for ICEEMDAN-RDPG revealed thirty-five components. In the case of standalone models, the PACF analysis of the AT, WSG, and RH time series generated three components. Two other variables including the GHI and the sunshine at the current time step are also included as an input to all the developed models. The sunshine variable is related to the presence or absence of solar irradiance and directly translates the state of the present framework. Solar irradiance is based on the sunshine hours, which are directly dependent on the sun. Therefore, we have considered the value of the sunshine variable as one, when the solar irradiance will exist. In the other situation, its value will correspond to zero. The addition of the sunshine variable adds intelligence to the forecasting model, and the lowest value (zero), as shown by this expert variable, generally demonstrates a night, while the peak value (one) typically reveals the center of a day with full sunshine. In short, the input features for the ISVR model are forty-eight, the VMD-RDPG and ICEEMDAN-RDPG models have twenty-four and thirty-seven input features, whereas the five input features are employed to develop the RDPG, LSTM, XGB, GPR, and SVR standalone models. The MinMaxScaler function of the Scikit-learn preprocessing module; is utilized for the normalization of data by transforming it between zero and one. Afterward, the transformed data is divided such that 80% of the total data is utilized for training, while the remaining 20% serves the purpose of testing.

E. MODELS CONSTRUCTION AND PARAMETER SELECTION

The purpose of this study is to forecast one-step ahead GHI based on a multivariate methodology by utilizing standalone, two-stage hybrid, and three-stage hybrid models. The selection of hyperparameters is an important step in the implementation of the MLMs. This study employs a manual search method for the selection of hyperparameters. For the SVR model, the selected hyperparameters include regularization parameter $=$ 10, epsilon $=$ 0.001, sigma $=$ 2.5, and the radial basis function kernel, which is also selected, for the GPR model. For XGB model, learning rate $= 10^{-1}$, min_child_weight $=$ 1, max_depth $=$ 15, colsample_bytree $=$ 0.8, n_estimators $=$ 200 are the selected hyperparameters. The LSTM model is employed with the following parameters: learning rate $= 10^{-3}$, optimizer $=$ Adam, hidden layer neurons $=$ 64, batch size $=$ 80. The state vector contains five, thirty-seven, twenty-four, and forty-eight features for ISVR, VMD-RDPG, ICEEMDAN-RDPG, and RDPG models. The forecasted GHI data are utilized as an action space. A reward function is included in the present study to determine the accuracy of forecasting. A zero value of the reward is obtained if the forecasted GHI is equal to the observed GHI value. However, if the forecasted GHI is different from the observed GHI, a negative reward would be received. Both actor and critic network are structured as a three layers architecture consisting of input, hidden, and the output layers and Adam optimizer is employed for actor and critic networks. The size of the input layer corresponds to the number of input features selected for each of these models, whereas the size of the output layer has a value of one. The number of hidden neurons in each of actor and critic networks is taken as 64, 150, 128, 200 for RDPG, ICEEMDAN-RDPG, VMD-RDPG, and ISVR models, respectively.

V. RESULTS AND COMPARATIVE ANALYSIS

Table 2 presents the RMSE, MAE, sMAPE, NSE, and d_r results for the proposed model and the benchmark models

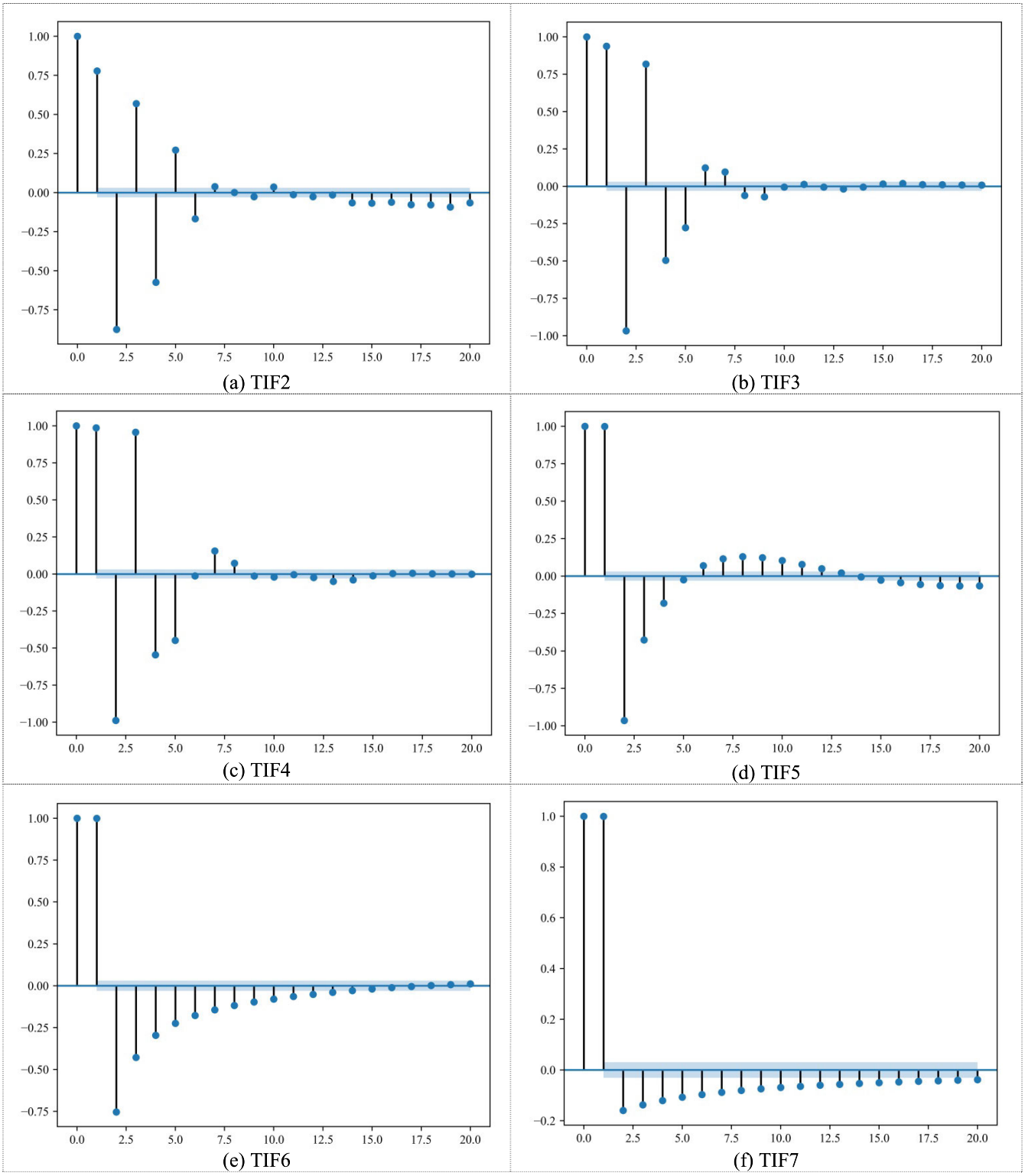


FIGURE 7. (A). PACF analysis of the AT series decomposed components for the ISVR model. (B). PACF analysis of the WSG series decomposed components for the ISVR model. (C). PACF analysis of the RH series decomposed components for the ISVR model.

during the training and testing periods. ISVR model outperformed all the comparison models with the lowest error values. Compared to the benchmark models, the ISVR model has reduced the RMSE values by 18.401 W/m^2 forVMD-RDPG, 13.908 W/m^2 for ICEEMDAN-RDPG, 33.223 W/m^2 for RDPG, 53.111 W/m^2 for LSTM, 67.704 W/m^2 for

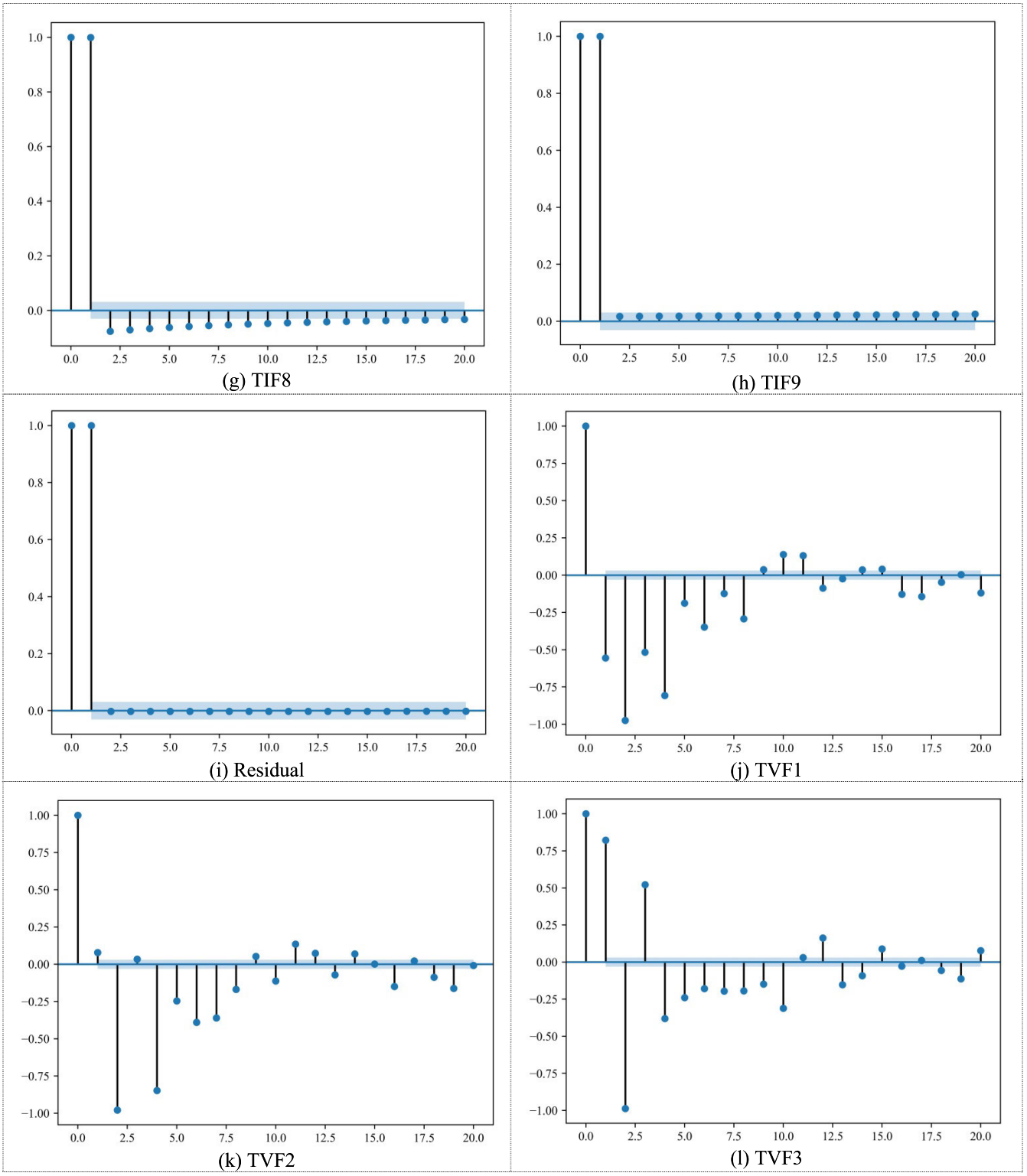
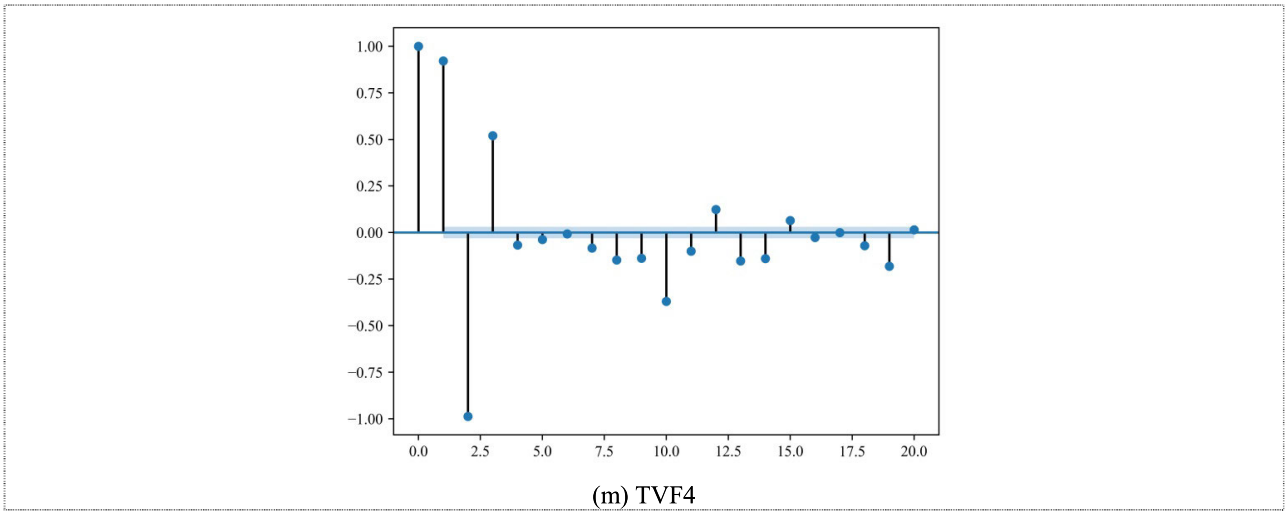


FIGURE 7. *(Continued.)* **(A). PACF analysis of the AT series decomposed components for the ISVR model. (B). PACF analysis of the WSG series decomposed components for the ISVR model. (C). PACF analysis of the RH series decomposed components for the ISVR model.**

XGB, 67.502 W/m^2 for GPR, 69.943 W/m^2 for SVR during the training period. Similarly, the reduced values of RMSE by the ISVR model compared to the other models include 17.463 W/m^2 for VMD-RDPG, 17.485 W/m^2 for ICEEMDAN-RDPG, 43.344 W/m^2 for RDPG, 45.829 W/m^2 for LSTM, 69.935 W/m^2 for XGB, 61.660 W/m^2 for GPR,



(A)

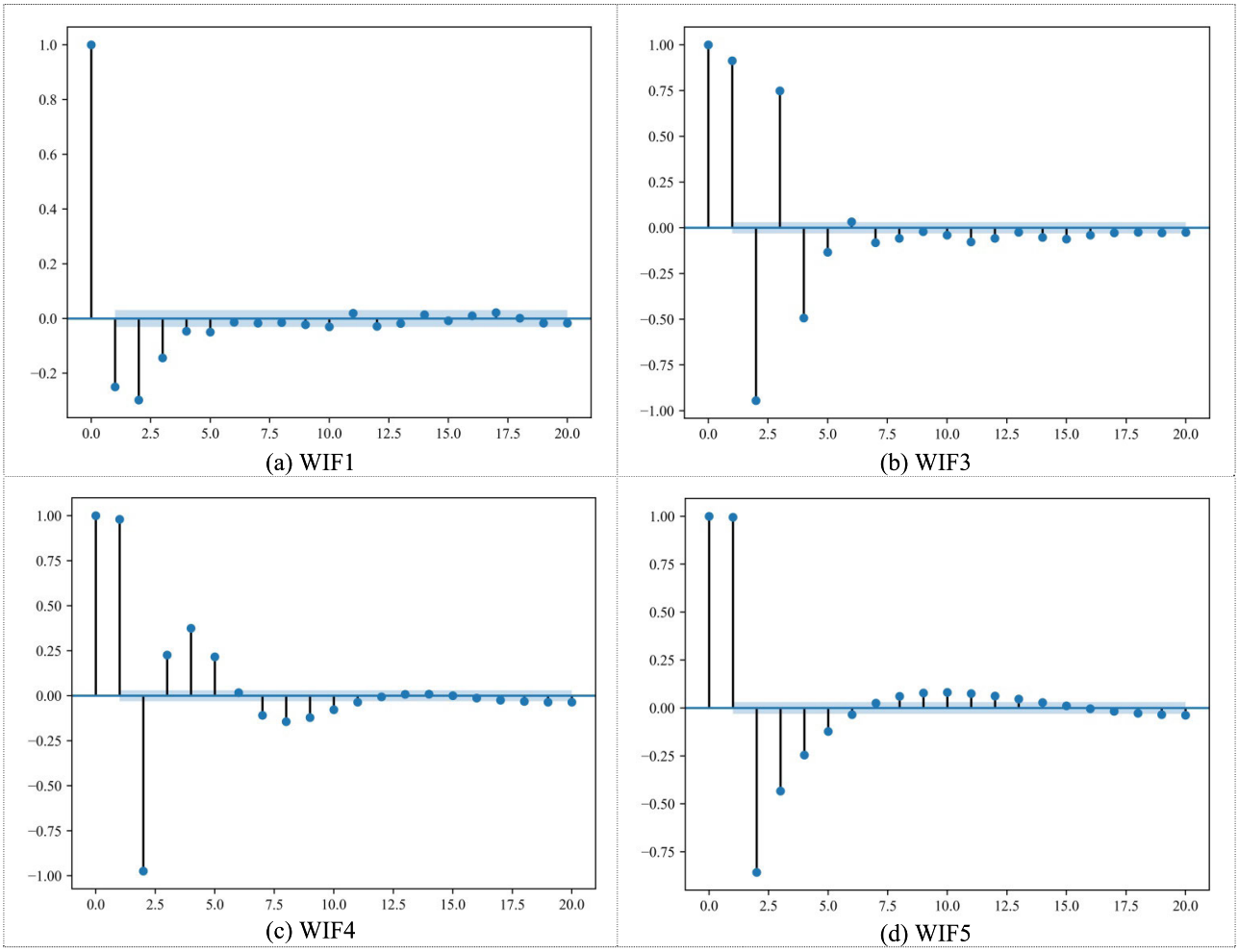


FIGURE 7. *(Continued.)* **(A). PACF analysis of the AT series decomposed components for the ISVR model. (B). PACF analysis of the WSG series decomposed components for the ISVR model. (C). PACF analysis of the RH series decomposed components for the ISVR model.**

66.520 W/m^2 for SVR during the testing period.VMD-RDPG and ICEEMDAN-RDPG also showed lower error values compared to the standalone models. The performance of the RDPG model is outstanding compared to the other standalone models. LSTM model also shows better forecasting results than the XGB, GPR, and SVR models.

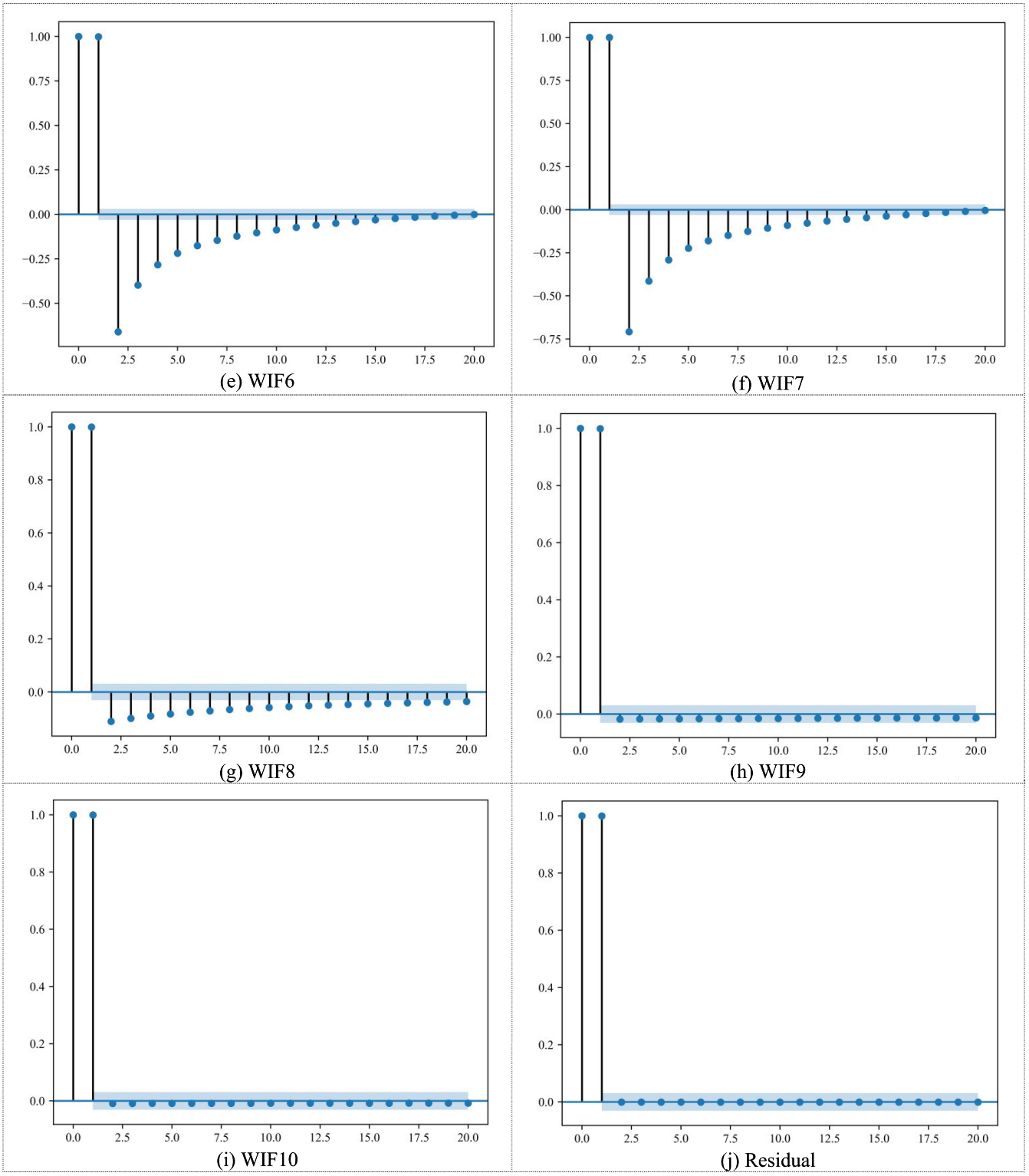
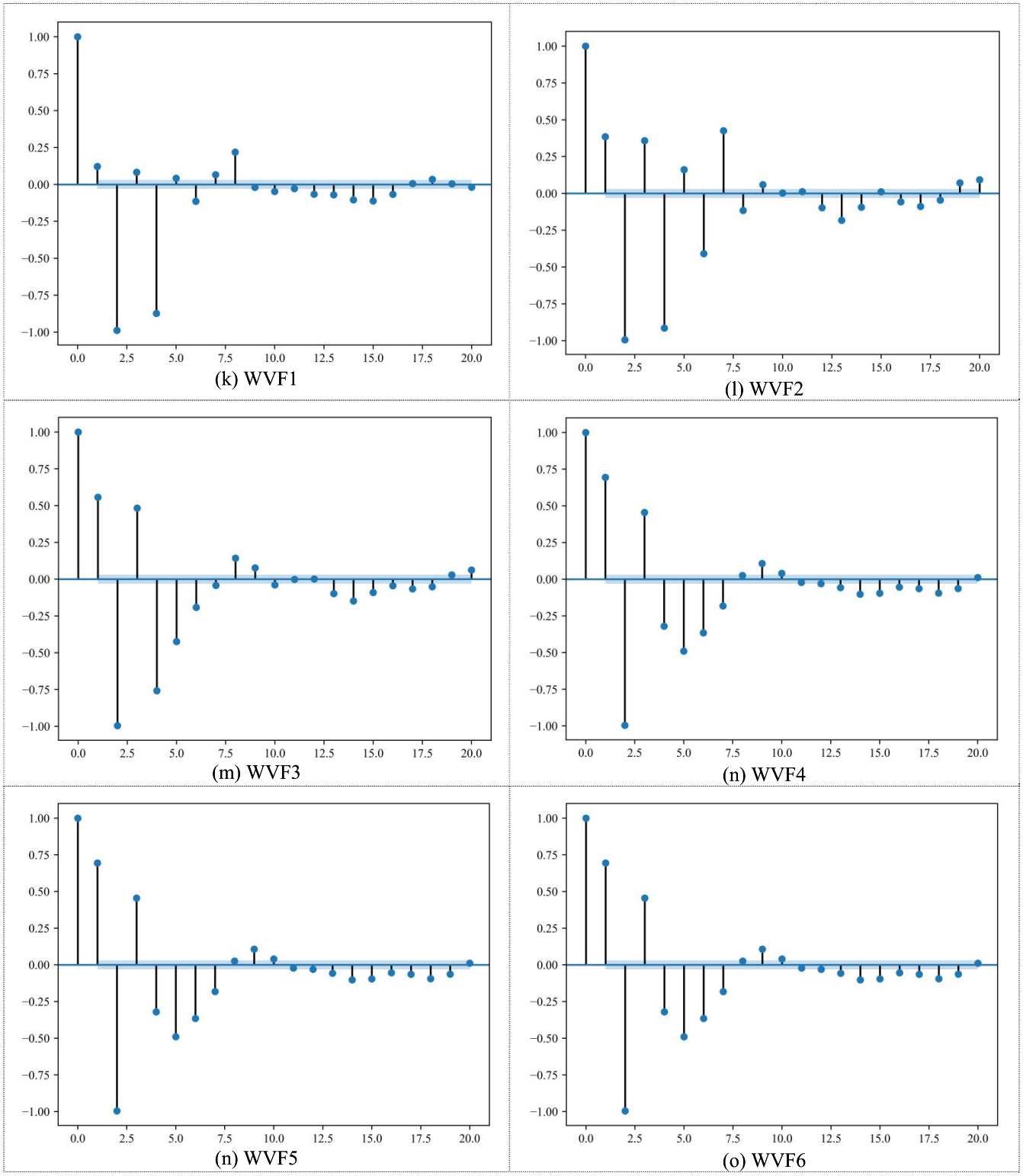


FIGURE 7. *(Continued.)* **(A). PACF analysis of the AT series decomposed components for the ISVR model. (B). PACF analysis of the WSG series decomposed components for the ISVR model. (C). PACF analysis of the RH series decomposed components for the ISVR model.**

The grander forecasting performance of the ISVR, VMD-RDPG, and ICEEMDAN-RDPG models is attributed to the viability of hybrid decomposition approaches and MLMs for GHI forecasting. The decomposition approaches extract nearly all the possible features from the time series to enhance the forecasting ability. Therefore, the models employing



(B)

FIGURE 7. *(Continued.)* **(A). PACF analysis of the AT series decomposed components for the ISVR model. (B). PACF analysis of the WSG series decomposed components for the ISVR model. (C). PACF analysis of the RH series decomposed components for the ISVR model.**

data-processing approaches result in significant reductions of error compared to the standalone MLMs without implementing decomposition techniques. The improved results of the LSTM and LSTM based RDPG models compared to the counterparts emphasize the practicability and robustness of the DL and RL methodologies for GHI forecasting.

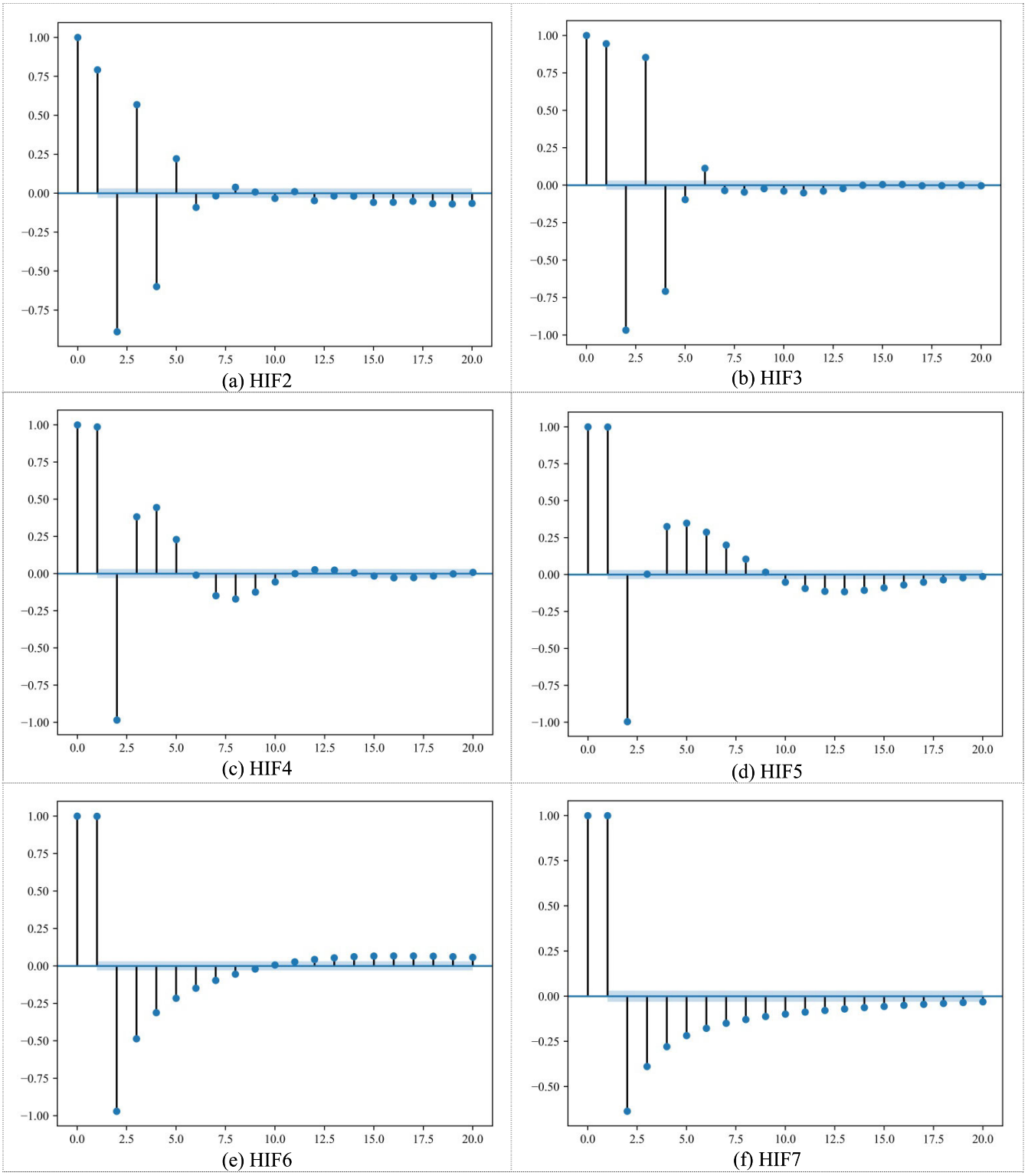


FIGURE 7. *(Continued.)* **(A). PACF analysis of the AT series decomposed components for the ISVR model. (B). PACF analysis of the WSG series decomposed components for the ISVR model. (C). PACF analysis of the RH series decomposed components for the ISVR model.**

The ISVR model effectively combines the benefits of ICEEMDAN, VMD, DL, and RL approaches, which results in its boosted performance over all the other developed models. The ICEEMDAN and VMD can efficiently investigate and decompose the observed data series to alleviate the non-stationary and non-linear features. Moreover, the strong

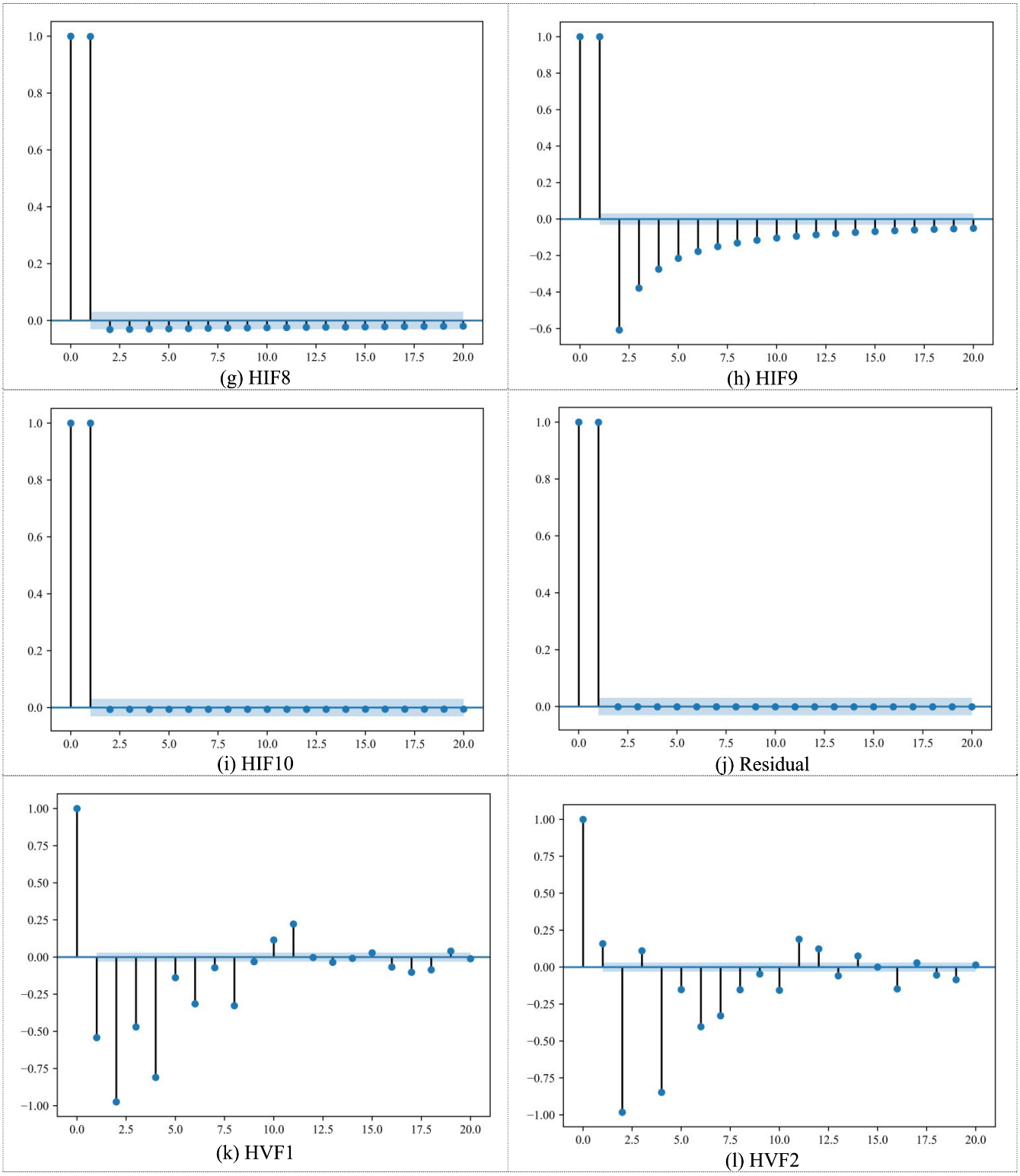
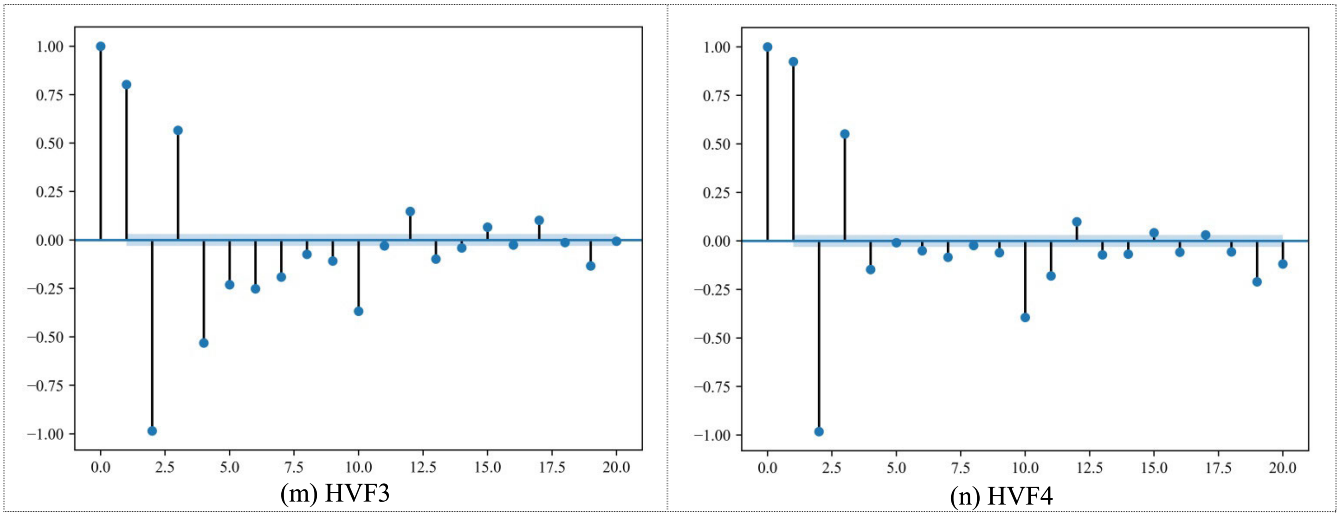


FIGURE 7. *(Continued.)* **(A). PACF analysis of the AT series decomposed components for the ISVR model. (B). PACF analysis of the WSG series decomposed components for the ISVR model. (C). PACF analysis of the RH series decomposed components for the ISVR model.**

decision-making capability of RL and the robust identification capability of the DL results in robust and enhanced performance of the ISVR. Thus, the ISVR model offers superior application prospects for GHI forecasting.

The mean and standard deviation of the RMSE and MAE metrics values are calculated to better evaluate the results. The square root transformation is applied to the non-normal RMSE and MAE data for computation



(C)

FIGURE 7. *(Continued.)* **(A). PACF analysis of the AT series decomposed components for the ISVR model. (B). PACF analysis of the WSG series decomposed components for the ISVR model. (C). PACF analysis of the RH series decomposed components for the ISVR model.**

TABLE 2. **Evaluation of the forecasting results using the developed models.**

Model	Training					Testing				
	RMSE (W/m^2)	MAE (W/m^2)	sMAPE (%)	NSE	d_r	RMSE (W/m^2)	MAE (W/m^2)	sMAPE (%)	NSE	d_r
SVR	122.845	80.360	38.958	0.860	0.820	123.707	82.530	39.375	0.858	0.813
GPR	120.404	80.912	37.962	0.872	0.834	118.847	80.134	38.737	0.869	0.826
XGB	120.606	78.918	36.207	0.896	0.863	121.122	81.150	38.262	0.885	0.861
LSTM	106.013	72.412	31.654	0.924	0.885	103.016	71.846	32.967	0.917	0.878
RDPG	86.125	60.841	29.213	0.938	0.890	100.531	68.843	29.457	0.933	0.883
ICEEMDAN-RDPG	66.810	38.982	26.414	0.957	0.930	74.672	46.361	26.757	0.948	0.921
VMD-RDPG	71.303	45.894	24.717	0.951	0.917	74.650	53.731	25.117	0.949	0.908
ISVR	**52.902**	**33.079**	**21.383**	**0.973**	**0.940**	**57.187**	**35.838**	**21.605**	**0.970**	**0.939**

of the mean and standard deviation values. During the training period, the mean values reported by the SVR, GPR, XGB, LSTM, RDPG, ICEEMDAN-RDPG, VMD-RDPG, and ISVR models are 17.604 W/m^2, 16.279 W/m^2, 17.023 W/m^2, 14.824 W/m^2, 13.974 W/m^2, 10.320 W/m^2, 11.541 W/m^2, and 9.984 W/m^2, respectively. Moreover, the SVR, GPR, XGB, LSTM, RDPG, ICEEMDAN-RDPG, VMD-RDPG, and ISVR models reveal standard deviation values of 8.831 W/m^2, 7.658 W/m^2, 7.341 W/m^2, 7.468 W/m^2, 7.334 W/m^2, 7.032 W/m^2, 7.099 W/m^2, and 5.713 W/m^2, respectively during the training period. According to the results, the ISVR model shows the lowest mean and standard deviation error values, which shows that most of the values are clustered around the mean compared to all the counterpart models. The SVR model shows the highest error values of mean and the standard deviation compared to all the other models indicating the highest variation in the data with a wider spread of values. Similarly, the mean and the standard deviation results during the testing period also show the lower error values for the hybrid models compared to standalone models. The ISVR model exemplifies the lowest mean and standard deviation error by displaying results of 10.231 W/m^2 and 6.223 W/m^2, respectively. The mean error values for the other models including SVR, GPR, XGB, LSTM, RDPG, ICEEMDAN-RDPG, and VMD-RDPG are 18.595 W/m^2, 18.047 W/m^2, 18.324 W/m^2, 15.853 W/m^2, 14.283 W/m^2, 12.514 W/m^2, and 12.981 W/m^2, respectively. Furthermore, the standard deviation error values for the SVR, GPR, XGB, LSTM, RDPG, ICEEMDAN-RDPG, and VMD-RDPG models are 9.570 W/m^2, 9.522 W/m^2, 9.274 W/m^2, 9.013 W/m^2, 8.453 W/m^2, 7.583 W/m^2, and 7.817 W/m^2, respectively.

The computational time of the SVR, GPR, XGB, LSTM, RDPG, ICEEMDAN-RDPG, VMD-RDPG, and ISVR models, is recorded as 0.370s, 0.092s, 0.452s, 79.901s, 215.101s, 1437.294s, 975.918s, and 1786.445s, respectively.

Among the standalone models, the LSTM and the LSTM based RDPG models are more computationally expensive compared to the other standalone models, which require very little execution time. The slower runtime performance of the RDPG model is due to the intricate training process of DL and RL involved in the RDPG model. Moreover, the runtimes of the hybrid models reveal larger values compared to all the standalone models, representing that these models are slower than the standalone models. The longer execution times of the hybrid models indicate that with the increase in the size of the dataset, the execution time of models also increases, making these models slower. Therefore, the ISVR model, with the largest size of the dataset, is the slowest compared to all the other developed models. On the other hand, the runtime gap between the ISVR model and the counterparts is decreasing, which also affirms the feasibility of the ISVR model for GHI forecasting.

The computational burden of the ISVR model mainly depends on the two factors. One includes the DRL based RDPG algorithm used in the ISVR model, involving both the DL and RL algorithms. The second comprises the large number of selected features used as an input to the RDPG algorithm in the ISVR model. The ISVR model utilizes more features compared to the other hybrid and standalone models. In the total computational time of 1786.445s by the ISVR model, the RDPG algorithm is the most computationally expensive and consumes 1694.030s. However, all the remaining steps of the ISVR model, including the correlation analysis, time series decomposition, and entropy calculation, takes only 92.415s. Therefore, it is evident that different steps contribute a little to the overall computational time of the ISVR model. This fact justifies the integration of ICEEMDAN, SE, PACF, VMD, and RDPG, to develop the ISVR model. Since the present study considers real case historical data, the performance of the model is expected to enhance in the real-time applications. More effective and relevant features can be extracted from the environment in real-time situations, which results in better training and the enhanced performance of the ISVR model. It may also lead to a decrease in computational time. For this reason, the DRL based hybrid models are also becoming popular in real-time environments with the advancements in artificial intelligence and increasing computational performance of the hardware system. Based on the above discussion, it can be inferred that the ISVR model can be applied to both online and offline forecasting of similar applications.

Contrary to the utilizations of DRL for control applications such as robotic, the implementation of DRL algorithms in forecasting mainly involves strategic decisions. In other words, the immediate implementation of forecasting decisions is not always mandatory. Therefore, the forecasting applications require accuracy, and computational delays are usually acceptable. Furthermore, the implementation of the RDPG model for different applications, which require a more rapid and accurate response compared to the forecasting, verifies the suitability of the RDPG. Consequently, the RDPG was applied to control traffic lights in transportation [73], learn adaptive behavior in driving [74], perform adaptive trading for different markets [75], and to reduce errors of robot positions and joint torques [42]. These applications of the RDPG algorithm signify that the RDPG based ISVR model is feasible for both offline and real-time applications in any type of complex environment.

The forecasting curves of all the established models are displayed in Fig. 8, which further demonstrates the forecasting performance.The red dotted line shows the observed GHI values, whereas other lines with different colors show the forecasted values by the proposed and the other counterpart models. The higher GHI values in Fig. 8 show the daytime when sunlight exists, while the lower values represent the night interval when sunlight is not available. The GHI values are decreasing as the time changes from day to night when sunlight is not available to reach its lowest values of zero somewhere in the middle of the night. Afterward, the GHI values are increasing from night to the middle of the day to experience their maximum values. In other words, it is apparent from Fig. 8 that the GHI pattern is following a typical real world day and night cycle. Therefore, the present study considers actual data for GHI forecasting, which demonstrates one of the advantages of this study. Fig. 8 (a), (c) shows the lower and zero values of GHI to illustrate a night; whereas, Fig. 8 (b) and (d) shows the peak GHI values for the mentioned periods to demonstrate a daytime. Consequently, in Fig. 8 (a), the time from 21:30 hours on 1/4/2016 to 03:50 hours on 2/4/2016 shows zero GHI values during the training period representing a night interval. Similarly, Fig. 8 (b) shows the peak GHI value of 960 W/m^2 at 12:40 hours on 1/7/2016, representing the daytime of a typical summer season. It is evident that the forecasted GHI curve of the ISVR is nearly similar to the observed GHI curve. The forecasting curves of the standalone models are quite different from the observed GHI curve. The SVR and GPR models are showing the least performance since their curves only roughly follow the observed GHI trend. Whereas, the hybrid models embedding decomposition techniques with the DRL approach outperform all the individual models, constructed without employing the signal decomposition processing. ISVR model is the most suitable model, and its curve reflects the observed GHI trend comparatively superior to the other established models. The ICEEMDAN-RDPG and VMD-RDPG models have also revealed better fitting curves at each point than the standalone models.

As a further investigation of the forecasting performance, Fig. 9 (A), (B) exhibits the scatter plots of all the constructed models during the training and testing periods. The ISVR model reveals the most uniformly distributed scatter points around the regression line compared to all the other models. Furthermore, the scatter points are almost nearest to the 1:1 line, which validates the applicability of the ISVR model compared to the other hybrid and standalone models. The scatter plots of the ICEEMDAN-RDPG and VMD-RDPG models also testify to their outclass performance over the

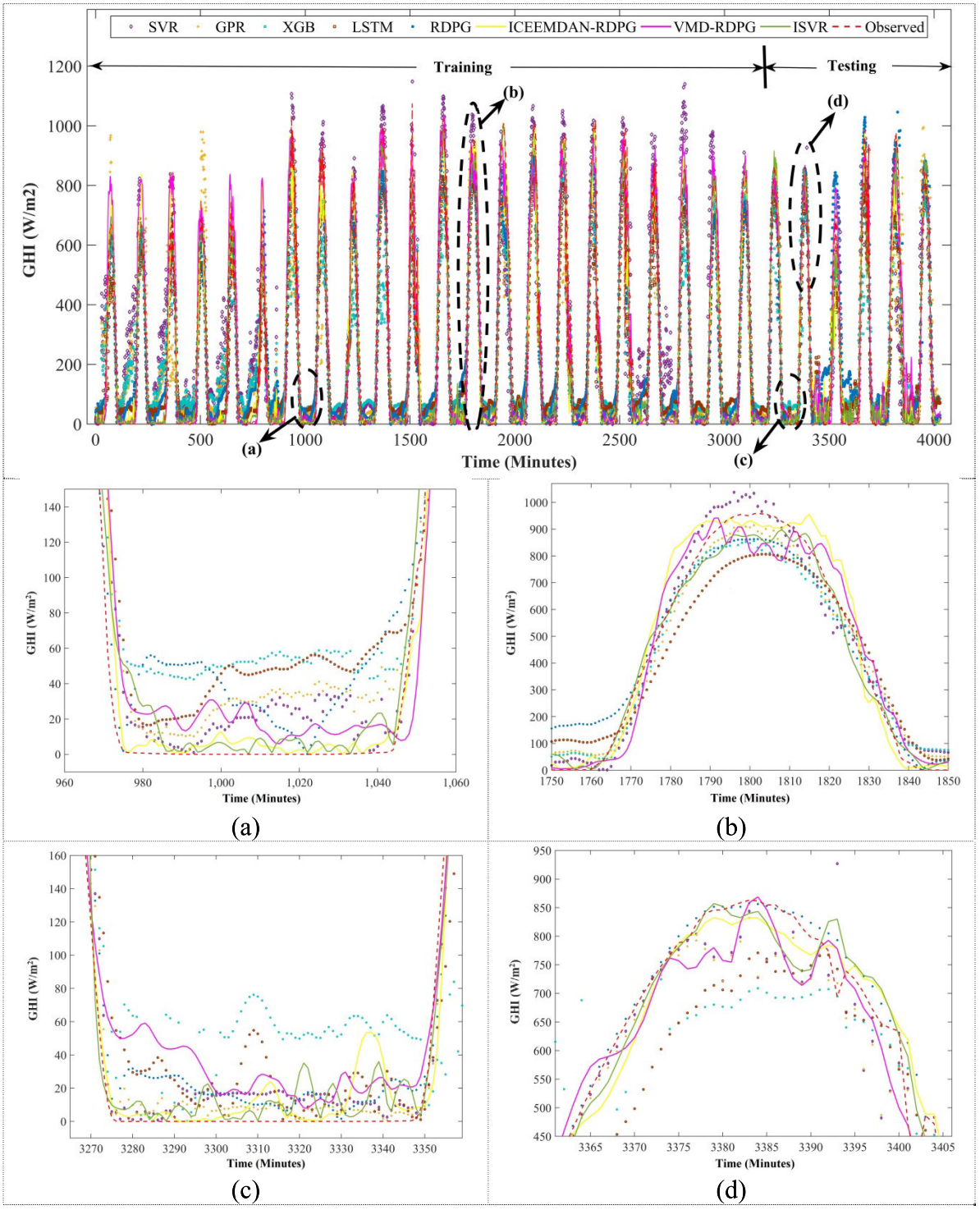
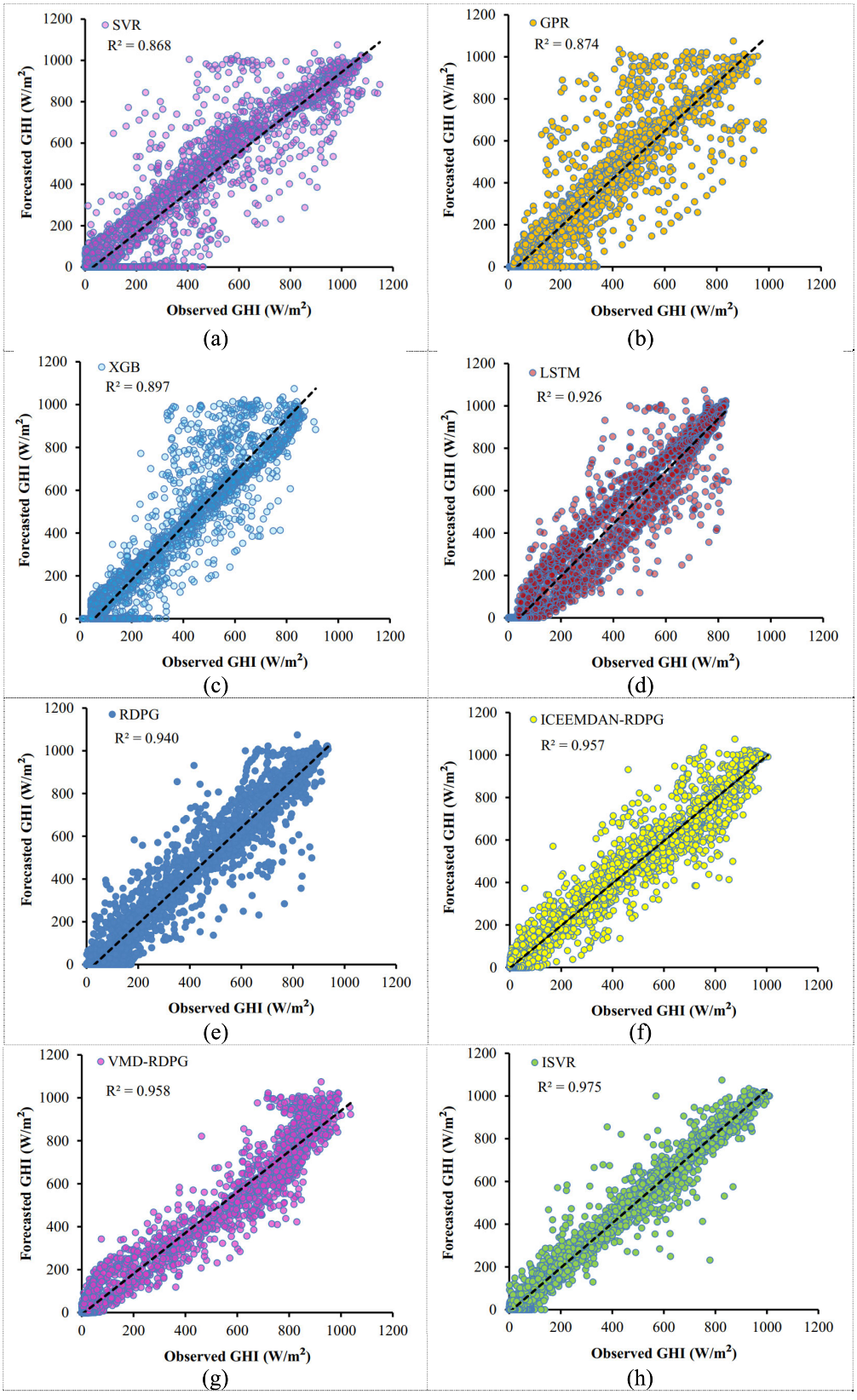


FIGURE 8. Comparison of the forecasting curves of the developed models with the observed GHI.

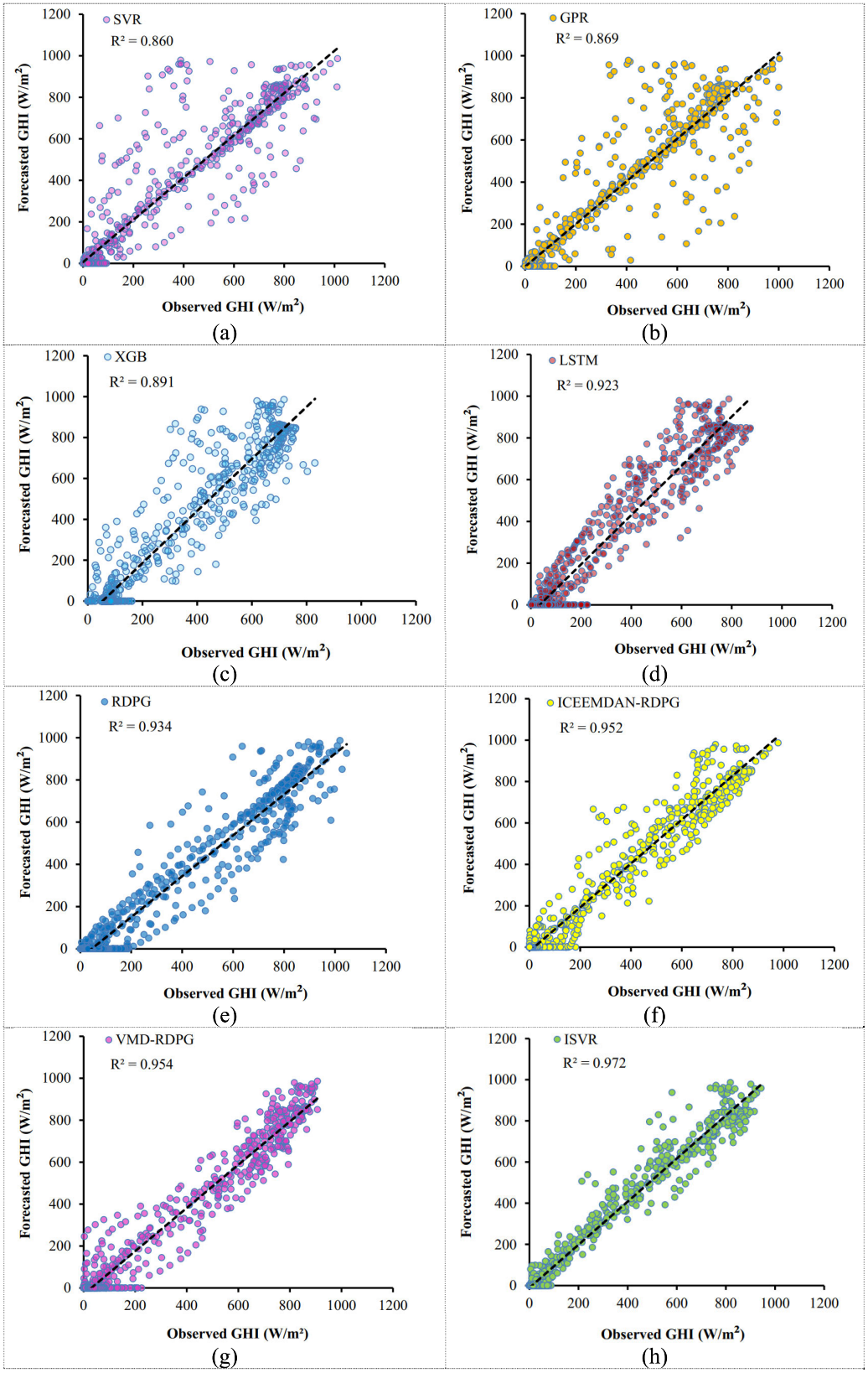
standalone models by presenting a more homogenous scattering pattern around the regression line. In the case of standalone models, the scatter plots of the LSTM and LSTM based RDPG model are more concentrated around the 1:1 line compared to the XGB, GPR, and SVR models, which have reflected a widespread scatter points around the regression line.

Fig. 10 (a), (b) evaluates the performance of different models by expressing the distribution of data in comparison with the observed dataset through violin plots. The violin



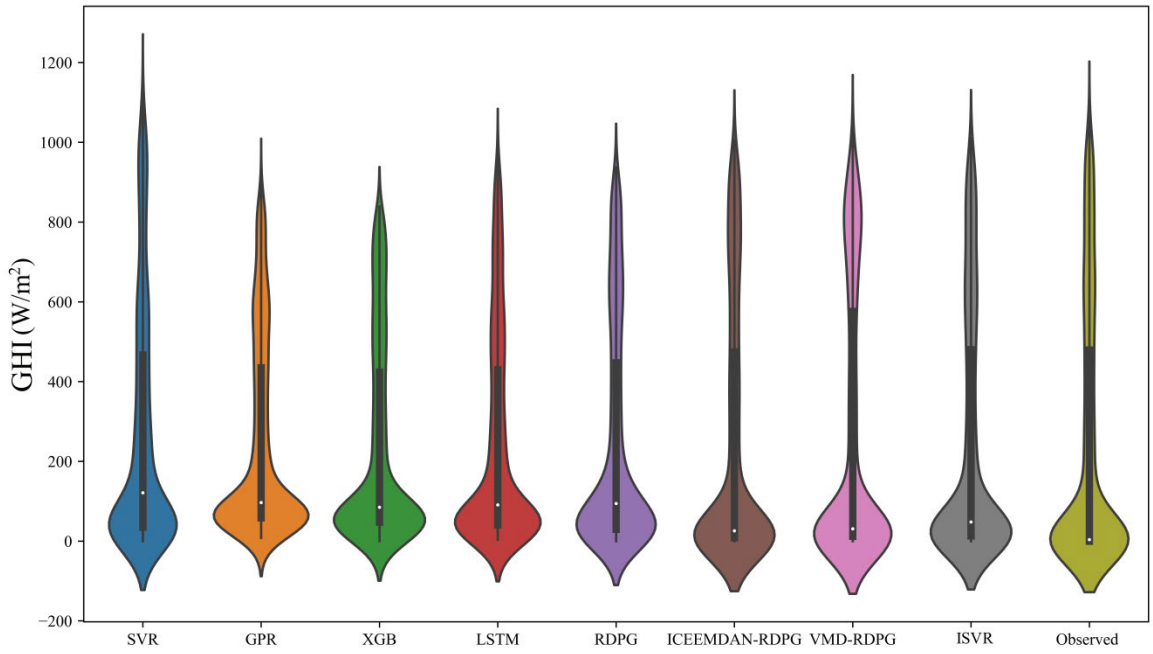
(A)

FIGURE 9. (A). Scatter plots of the developed models during the training period. (B). Scatter plots of the developed models during the testing period.

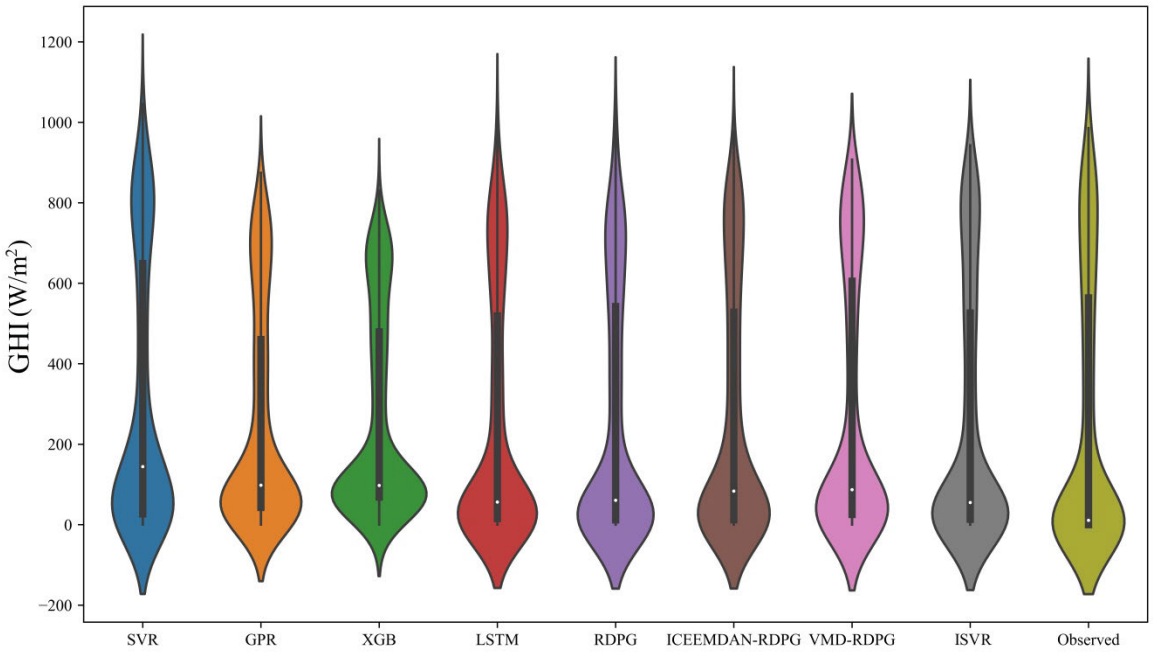


(B)

FIGURE 9. *(Continued.)* **(A). Scatter plots of the developed models during the training period. (B). Scatter plots of the developed models during the testing period.**



(a) The training period.



(b) The testing period.

FIGURE 10. Violin plots to show the comparison of the developed models in forecasting GHI. (a) The training period, (b) The testing period.

plots of the hybrid models yield more similar data distribution with the observed dataset. Moreover, the boxplot quartiles of the hybrid models have shown a nearly matched spread of forecasted data with the observed data compared to the standalone MLMs. The location of the median is right-skewed for all the developed models, which resembles the observed data and signifies the applicability of the MLMs for GHI forecasting. During the testing period, the mean values of forecasted GHI shown by SVR, GPR, XGB, LSTM, RDPG, ICEEMDAN-RDPG, VMD-RDPG, and ISVR are 309.010 W/m^2, 251.952 W/m^2, 254.785 W/m^2, 245.167 W/m^2, 253.997 W/m^2, 260.171 W/m^2, 278.107 W/m^2, and 255.105 W/m^2, respectively, against the observed GHI mean value of 255.775 W/m^2.

Furthermore, corresponding to the median value of 10.750 W/m^2 for the observed GHI data, the SVR, GPR, XGB, LSTM, RDPG, ICEEMDAN-RDPG, VMD-RDPG, and ISVR models have depicted the median values of 144.313 W/m^2, 97.965 W/m^2, 97.558 W/m^2, 56.310 W/m^2, 60.677 W/m^2, 83.576 W/m^2, 86.854 W/m^2, and 54.912 W/m^2, respectively. The values of lower and upper quartiles and the interquartile ranges portrayed by the hybrid models are close to the observed data compared to the standalone models. Similar to the testing period, the boxplot and the probability density of the observed data during the training period are in close agreement with the hybrid models in contrast to the individual MLMs. The hybrid models are more feasible to capture the non-stationary and non-linear dynamics of observed data compared to the standalone MLMs. Although the standalone MLMs could perform the task of forecasting, they are less accurate and effectual than the hybrid models.

Fig. 11 (a), (b) illustrates the comparison of RMSE distribution for all models. The RDPG based models evidence the lower values of error compared to the standalone SVR, GPR, XGB, and LSTM models. Among the hybrid models, the error values of the ISVR model are comparatively lower than the ICEEMDAN-RDPG and VMD-RDPG hybrid models. The error values of the IVSR model are mostly confined, in the lower region, compared to the benchmark models. Among the standalone models, the LSTM and the LSTM based RDPG model revealed the smallest values of error points compared to the SVR, GPR, and XGB standalone models. This fact enlightens the superiority and the applicabilit; of the DL and RL approaches for GHI forecasting. The error distribution results again show the advantages of DRL and decomposition approaches in enhancing the performance of the MLMs for forecasting purposes. The overall ranking of the developed models considering the displayed results in ascending order is SVR, GPR, XGB, LSTM, RDPG, ICEEMDAN-RDPG, VMD-RDPG, and ISVR.

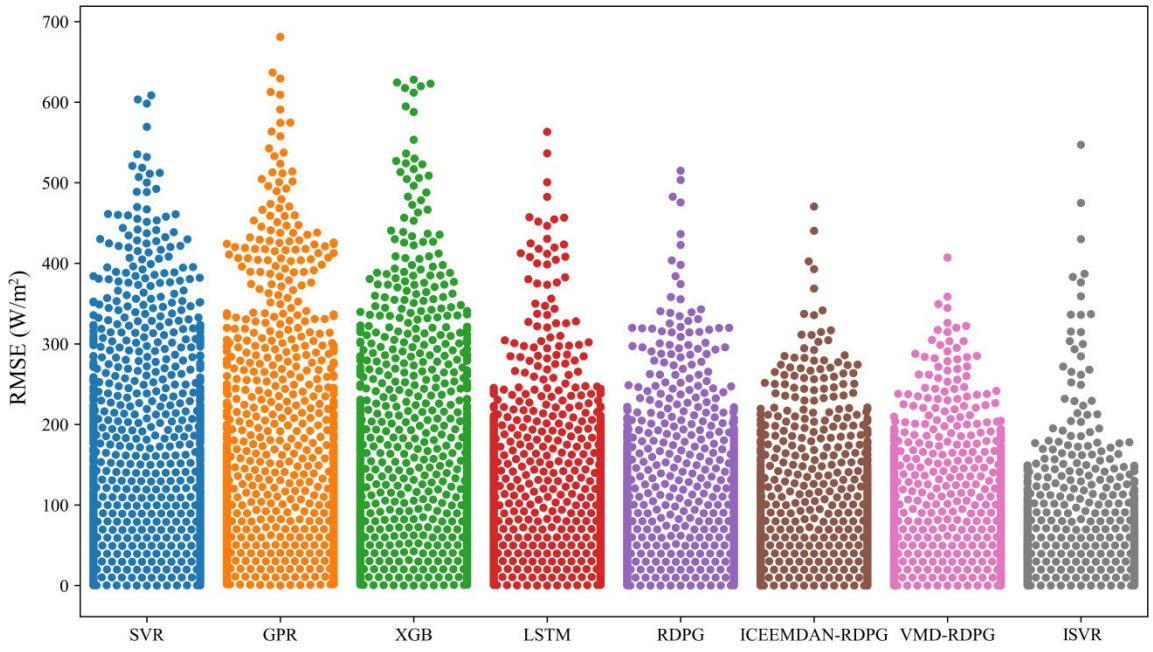
In short, the integration of ICEEMDAN and VMD processing techniques with the LSTM based DRL approach can boost the precision of the hybrid GHI forecasting models. The present study applies the ISVR model to forecast GHI based on multivariate time series data. In reality, the ISVR model is feasible to perform a forecast of any types of time series problems, such as wind power, electrical load, C_{O2} emissions, and drought.

Regardless of the superior forecasting results shown by the developed models, this study reveals some limitations and challenges, which may be addressed in future studies.

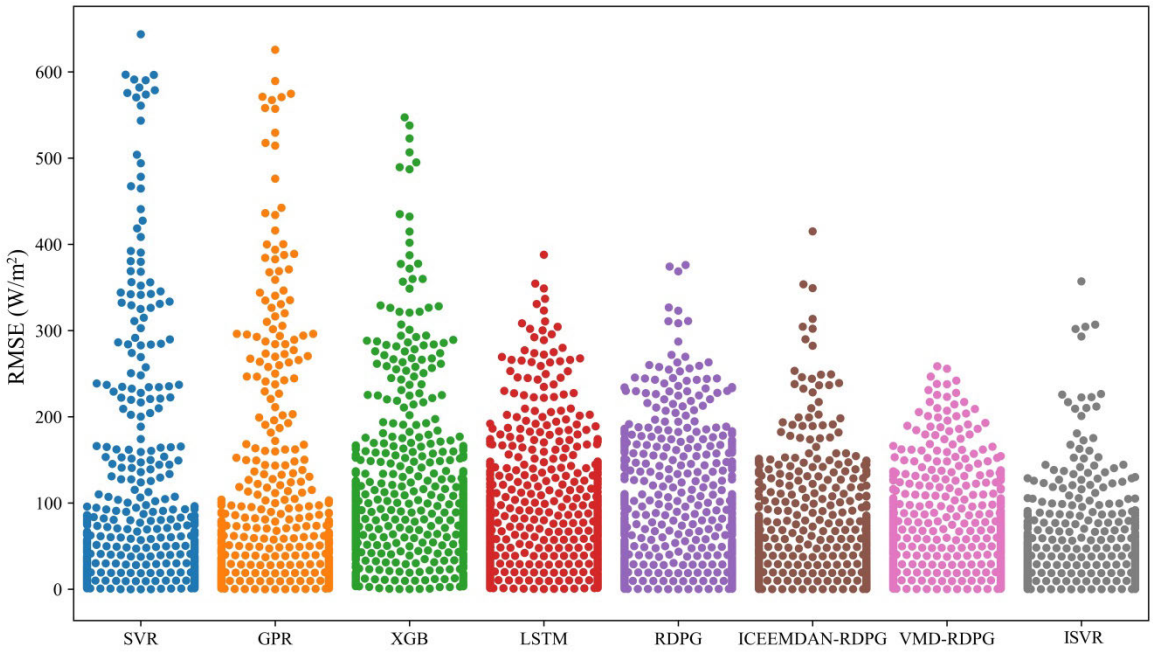
Firstly, the accurate forecasting of GHI is a challenging task due to the stochastic and non-stationary nature of solar irradiance and the associated variables. This fact limits the capability of our proposed model to forecast GHI with 100% accuracy despite the availability of reliable data. This uncertain condition requires the exploration of novel solar irradiance forecasting techniques to ameliorate the capability of our proposed model and to cope with the challenge of environmental uncertainty in a more efficient way.

Secondly, the present study has applied the RL by considering a straightforward situation, i.e., the historical multivariate meteorological data forecast the historical GHI, without consideration of other RERs or connection with the power grid. The design and implementation of DRL methodologies for forecasting and control of RERs on a broad scale is a complex process. Moreover, managing ADNs involving numerous RERs in a time-varying condition is a challenging task [76]. Hence, to extend the present forecasting framework for ADNs, online ADNs optimization and management techniques are necessary. The computationally affordable online convex optimization [76]; can be applied for economic dispatch of transmission system [77], as a feedback controller for RERs [78], and to coordinate microgrids and RERs [79]. Robust and incentive-based coordination of RER; can be achieved by applying the Lyapunov optimization-based online distributed approach [76]. The reliability and the flexibility of the power system can be augmented by an energy storage system with the provision of auxiliary services, including energy arbitrage, frequency and voltage regulation, black start support, and reverse power [80]. The above implementations demonstrate the viability of online approaches for flexible integration and management of RERs, energy storage system, and secondary services offered by these systems. Therefore, the proposed forecasting model can be extended, in the future, to check its applicability for ADNs, which are paramount to seamlessly integrate RERs and energy storage system for a reliable operation and planning of the power system.

Thirdly, the increasing numbers of worse cyberattacks are jeopardizing the security and functional reliability of power systems [81]. Since the present study only forecast GHI without integration with the grid or distribution system, therefore, the GHI forecasting model has not employed the cyberattack parameter and its consequences. However, the consideration of cyberattacks is necessary, especially in the case of RER integration with the grid. Even for the present study, being conducted on a small scale, the cyberattacks still can affect the data extraction system associated with the measuring instruments. The aurora vulnerability and the attack on the power grid of Ukraine provide examples of a cyberattack on the power system. A malicious actor can inadvertently reprogram the network-enabled and reconfigurable devices by acting remotely, resulting in the physical destruction of the infrastructure and equipment. Therefore, the detection of cyberattacks is necessary to protect the equipment damage and for a secure and reliable operation of the industrial control system [82]. The susceptance and the reactance of transmission lines can be actively changed for hiding parameters in the moving-target-defense approach to prevent and mitigate cyberattacks. The moving-target-defense approach circumvented cyberattacks by hiding the line susceptance of transmission lines [83], self and mutual reactance of transmission lines [84], and the branch reactance of the alternating current



(a) The training period.



(b) The testing period.

FIGURE 11. Comparison of RMSE distribution for all the developed models. (a) The training period, (b) The testing period.

network [85]. The frequency control of the power system was also studied by considering the load altering type of cyberattacks, and the corresponding RL based defense approaches improved the performance of frequency control [86]. The vulnerability of cyberattacks for power systems also demands to consider and forecast cyberattacks and their consequences in the establishment of secure power systems and smart grids of the future.

Fourthly, the present study considers GHI forecasting by considering meteorological data with a resolution in minutes.

However, the other time scales, such as hourly, daily, weekly, and monthly, can be employed to compare the performance of the proposed model with different time steps.

Lastly, despite the viability of decomposition-based data pre-processing approaches in embedded configuration with forecasting models, the generation of a large number of modes adds to the complexity of the forecasting models. Furthermore, the DRL models are computationally expensiv; compared to the other MLMs. These limitations necessitate the development of novel methods to deal with the situation, which can help in reducing the computational burden of the forecasting models.

VI. CONCLUSION

Solar irradiance can play a significant role to fulfill the global demand for energy with prospects of renewable, clean, and accessible solar energy source. Hence, this study attempts to forecast GHI by developing the ISVR mode. The ICEEMDAN-SE-VMD-RDPG model is constructed by integrating ICEEMDAN, SE, VMD, and RDPG. Firstly, the correlation between multivariate meteorological data is determined by the Pearson correlation coefficient to reduce the redundant data. ICEEMDAN is applied subsequently to decompose the data into different modes to lessen the non-stationarity. Afterward, VMD is adopted to execute the secondary decomposition of the ICEEMDAN modal component with the highest value of SE. PACF analysis of the obtained modes is performed subsequently for feature extraction and input selection for the DRL models. Finally, the LSTM based RDPG is employed to complete the GHI forecasting process. Two-hybrid models (ICEEMDAN-RDPG and VMD-RDPG), and five standalone models (RDPG, LSTM, XGB, GPR, and SVR), are developed to provide a comparative analysis with the ISVR model. The experimental results reveal that

1) Pearson correlation coefficient can be effectively applied to remove the redundant data.
2) The standalone RDPG model has a higher forecasting accuracy than the standalone LSTM, XGB, GPR, and SVR models, which testifies the superiority and the applicability of the LSTM based DRL model over the other developed MLMs.
3) Two-stage hybrid models, including ICEEMDAN-RDPG and VMD-RDPG, involving a single decomposition stage (ICEEMDAN and VMD), are superior in performance to the standalone models. The decomposition approaches result in the improvement of the hybrid models over the standalone models.
4) SE can be employed to determine the signal complexity. Moreover, PACF analysis is viable to extract features of the time series.
5) A secondary decomposition stage enhances the forecasting ability of the hybrid models with a single decomposition stage. Therefore, the integration of ICEEMDAN and VMD techniques has resulted in the superior performance of the ICEEMDAN-SE-VMD-RDPG model.

In a nutshell, the proposed model can be appropriately applied to solar irradiance forecasting. Accurate GHI forecasting is vital in identifying the future possibilities of solar energy, effective resource utilization, and reliable planning. The present study considers the data of Pakistan for forecasting purpose. In reality, owing to the flexibility and advantages of the DDMs over the process driven models, the proposed hybrid model based on the data driven approach is also equally applicable to the other parts of the world. This method can be applied in any location where relevant meteorological parameters are measured. Moreover, the proposed model is also suitable for the forecasting of other time series problems; thereby, delivering wide-range application prospects. Some examples include forecasting of load demand, the complementarity of RERs, environment monitoring, natural disasters, and epidemics, thus offering benefits for better utilization of resources, effective planning and improved decision-making, development of early warning systems, and enhanced coordination and control. Future research will develop new forecasting models by considering the strengths, limitations, and prospects of the proposed model for a secure, flexible, and economic integration and management of RERs into the power system.

REFERENCES

[1] S. Stökler, C. Schillings, and B. Kraas, "Solar resource assessment study for Pakistan," *Renew. Sustain. Energy Rev.*, vol. 58, pp. 1184–1188, May 2016.
[2] M. A. Sheikh, "Renewable energy resource potential in Pakistan," *Renew. Sustain. Energy Rev.*, vol. 13, no. 9, pp. 2696–2702, Dec. 2009.
[3] I. Ulfat, F. Javed, F. A. Abbasi, F. Kanwal, A. Usman, M. Jahangir, and F. Ahmed, "Estimation of solar energy potential for Islamabad, Pakistan," *Energy Procedia*, vol. 18, pp. 1496–1500, Jan. 2012.
[4] K. H. Solangi, M. R. Islam, R. Saidur, N. A. Rahim, and H. Fayaz, "A review on global solar energy policy," *Renew. Sustain. Energy Rev.*, vol. 15, no. 4, pp. 2149–2163, May 2011.
[5] R. Srivastava, A. N. Tiwari, and V. K. Giri, "Solar radiation forecasting using MARS, CART, m5, and random forest model: A case study for india," *Heliyon*, vol. 5, no. 10, Oct. 2019, Art. no. e02692.
[6] J. Chang, Y. Du, X. Chen, E. G. Lim, and K. Yan, "Forecasting based virtual inertia control of PV systems for islanded micro-grid," in *Proc. 29th Australas. Universities Power Eng. Conf. (AUPEC)*, Nov. 2019, pp. 1–6.
[7] C. Voyant, G. Notton, S. Kalogirou, M.-L. Nivet, C. Paoli, F. Motte, and A. Fouilloy, "Machine learning methods for solar radiation forecasting: A review," *Renew. Energy*, vol. 105, pp. 569–582, May 2017.
[8] R. Prasad, M. Ali, P. Kwan, and H. Khan, "Designing a multi-stage multivariate empirical mode decomposition coupled with ant colony optimization and random forest model to forecast monthly solar radiation," *Appl. Energy*, vol. 236, pp. 778–792, Feb. 2019.
[9] Y. Gala, Á. Fernández, J. Díaz, and J. R. Dorronsoro, "Hybrid machine learning forecasting of solar radiation values," *Neurocomputing*, vol. 176, pp. 48–59, Feb. 2016.
[10] V. H. Quej, J. Almorox, J. A. Arnaldo, and L. Saito, "ANFIS, SVM and ANN soft-computing techniques to estimate daily global solar radiation in a warm sub-humid environment," *J. Atmos. Solar-Terrestrial Phys.*, vol. 155, pp. 62–70, Mar. 2017.
[11] K. Angela, S. Taddeo, and M. James, "Predicting global solar radiation using an artificial neural network single-parameter model," *Advances in Artificial Neural Systems*, vol. 2011, Nov. 2011, Art. no. 751908 .
[12] S. M. Al-Alawi and H. A. Al-Hinai, "An ANN-based approach for predicting global radiation in locations with no direct measurement instrumentation," *Renew. Energy*, vol. 14, nos. 1–4, pp. 199–204, May 1998.
[13] J. Li, J. K. Ward, J. Tong, L. Collins, and G. Platt, "Machine learning for solar irradiance forecasting of photovoltaic system," *Renew. Energy*, vol. 90, pp. 542–553, May 2016.

[14] L. M. Aguiar, B. Pereira, M. David, F. Díaz, and P. Lauret, "Use of satellite data to improve solar radiation forecasting with Bayesian artificial neural networks," *Sol. Energy*, vol. 122, pp. 1309–1324, Dec. 2015.
[15] L. Benali, G. Notton, A. Fouilloy, C. Voyant, and R. Dizene, "Solar radiation forecasting using artificial neural network and random forest methods: Application to normal beam, horizontal diffuse and global components," *Renew. Energy*, vol. 132, pp. 871–884, Mar. 2019.
[16] V. Vapnik, *The Nature of Statistical Learning Theory*. New York, NY, USA: Springer, 2000. [Online]. Available: https://link.springer.com/book/10.1007%2F978-1-4757-3264-1#about
[17] J.-L. Chen and G.-S. Li, "Evaluation of support vector machine for estimation of solar radiation from measured meteorological variables," *Theor. Appl. Climatol.*, vol. 115, nos. 3–4, pp. 627–638, Feb. 2014.
[18] J. Fan, L. Wu, F. Zhang, H. Cai, W. Zeng, X. Wang, and H. Zou, "Empirical and machine learning models for predicting daily global solar radiation from sunshine duration: A review and case study in China," *Renew. Sustain. Energy Rev.*, vol. 100, pp. 186–212, Feb. 2019.
[19] R. Urraca, E. Martinez-de-Pison, A. Sanz-Garcia, J. Antonanzas, and F. Antonanzas-Torres, "Estimation methods for global solar radiation: Case study evaluation of five different approaches in central Spain," *Renew. Sustain. Energy Rev.*, vol. 77, pp. 1098–1113, Sep. 2017.
[20] J. Fan, X. Wang, L. Wu, H. Zhou, F. Zhang, X. Yu, X. Lu, and Y. Xiang, "Comparison of support vector machine and extreme gradient boosting for predicting daily global solar radiation using temperature and precipitation in humid subtropical climates: A case study in China," *Energy Convers. Manage.*, vol. 164, pp. 102–111, May 2018.
[21] M. Guermoui, K. Gairaa, A. Rabehi, D. Djafer, and S. Benkaciali, "Estimation of the daily global solar radiation based on the Gaussian process regression methodology in the Saharan climate," *Eur. Phys. J. Plus*, vol. 133, no. 6, p. 211, Jun. 2018.
[22] F. Lubbe, J. Maritz, and T. Harms, "Evaluating the potential of Gaussian process regression for solar radiation forecasting: A case study," *Energies*, vol. 13, no. 20, p. 5509, Oct. 2020.
[23] J. Yuan, K. Wang, T. Yu, and M. Fang, "Reliable multi-objective optimization of high-speed WEDM process based on Gaussian process regression," *Int. J. Mach. Tools Manuf.*, vol. 48, no. 1, pp. 47–60, Jan. 2008.
[24] Y. Liu and Z. Gao, "Real-time property prediction for an industrial rubber-mixing process with probabilistic ensemble Gaussian process regression models," *J. Appl. Polym. Sci.*, vol. 132, no. 6, p. 41432, Feb. 2015.
[25] T. Chen and C. Guestrin, "XGBoost: A scalable tree boosting system," in *Proc. 22nd ACM SIGKDD Int. Conf. Knowl. Discovery Data Mining*, Aug. 2016, pp. 785–794.
[26] X. Qing and Y. Niu, "Hourly day-ahead solar irradiance prediction using weather forecasts by LSTM," *Energy*, vol. 148, pp. 461–468, Apr. 2018.
[27] B. Gao, X. Huang, J. Shi, Y. Tai, and R. Xiao, "Predicting day-ahead solar irradiance through gated recurrent unit using weather forecasting data," *J. Renew. Sustain. Energy*, vol. 11, no. 4, Jul. 2019, Art. no. 043705.
[28] J. Wojtkiewicz, M. Hosseini, R. Gottumukkala, and T. L. Chambers, "Hour-ahead solar irradiance forecasting using multivariate gated recurrent units," *Energies*, vol. 12, no. 21, p. 4055, Oct. 2019.
[29] K. Yan, H. Shen, L. Wang, H. Zhou, M. Xu, and Y. Mo, "Short-term solar irradiance forecasting based on a hybrid deep learning methodology," *Information*, vol. 11, no. 1, p. 32, Jan. 2020.
[30] H. Zhou, Y. Zhang, L. Yang, Q. Liu, K. Yan, and Y. Du, "Short-term photovoltaic power forecasting based on long short term memory neural network and attention mechanism," *IEEE Access*, vol. 7, pp. 78063–78074, 2019.
[31] S. Singaravel, J. Suykens, and P. Geyer, "Deep-learning neural-network architectures and methods: Using component-based models in building-design energy prediction," *Adv. Eng. Informat.*, vol. 38, pp. 81–90, Oct. 2018.
[32] C. Fan, Y. Sun, Y. Zhao, M. Song, and J. Wang, "Deep learning-based feature engineering methods for improved building energy prediction," *Appl. Energy*, vol. 240, pp. 35–45, Apr. 2019.
[33] T. Liu, C. Xu, Y. Guo, and H. Chen, "A novel deep reinforcement learning based methodology for short-term HVAC system energy consumption prediction," *Int. J. Refrig.*, vol. 107, pp. 39–51, Nov. 2019.
[34] H. Liu, C. Yu, H. Wu, Z. Duan, and G. Yan, "A new hybrid ensemble deep reinforcement learning model for wind speed short term forecasting," *Energy*, vol. 202, Jul. 2020, Art. no. 117794.
[35] D. Elavarasan and P. M. D. Vincent, "Crop yield prediction using deep reinforcement learning model for sustainable agrarian applications," *IEEE Access*, vol. 8, pp. 86886–86901, 2020.
[36] R.-J. Park, K.-B. Song, and B.-S. Kwon, "Short-term load forecasting algorithm using a similar day selection method based on reinforcement learning," *Energies*, vol. 13, no. 10, p. 2640, May 2020.
[37] E. Oh and H. Wang, "Reinforcement-learning-based energy storage system operation strategies to manage wind power forecast uncertainty," *IEEE Access*, vol. 8, pp. 20965–20976, 2020.
[38] C. Chen, M. Cui, F. Li, S. Yin, and X. Wang, "Model-free emergency frequency control based on reinforcement learning," *IEEE Trans. Ind. Informat.*, vol. 17, no. 4, pp. 2336–2346, Apr. 2021.
[39] L. P. Tuyen and T. Chung, "Controlling bicycle using deep deterministic policy gradient algorithm," in *Proc. 14th Int. Conf. Ubiquitous Robots Ambient Intell. (URAI)*, Jun. 2017, pp. 413–417.
[40] T. P. Lillicrap, J. J. Hunt, A. Pritzel, N. Heess, T. Erez, Y. Tassa, D. Silver, and D. Wierstra, "Continuous control with deep reinforcement learning," 2015, *arXiv:1509.02971*. [Online]. Available: https://arxiv.org/abs/1509.02971
[41] N. Heess, J. J. Hunt, T. P. Lillicrap, and D. Silver, "Memory-based control with recurrent neural networks," 2015, *arXiv:1512.04455*. [Online]. Available: http://arxiv.org/abs/1512.04455
[42] Y. Li, S. Guo, L. Zhu, T. Mukai, and Z. Gan, "A recurrent reinforcement learning approach applicable to highly uncertain environments," *Int. J. Adv. Robotic Syst.*, vol. 17, no. 2, 2020, Art. no. 1729881420916258.
[43] M. Rezaie-Balf, N. Maleki, S. Kim, A. Ashrafian, F. Babaie-Miri, N. W. Kim, I.-M. Chung, and S. Alaghmand, "Forecasting daily solar radiation using CEEMDAN decomposition-based MARS model trained by crow search algorithm," *Energies*, vol. 12, no. 8, p. 1416, Apr. 2019.
[44] R. Prasad, M. Ali, Y. Xiang, and H. Khan, "A double decomposition-based modelling approach to forecast weekly solar radiation," *Renew. Energy*, vol. 152, pp. 9–22, Jun. 2020.
[45] H. Lan, H. Yin, Y.-Y. Hong, S. Wen, D. C. Yu, and P. Cheng, "Day-ahead spatio-temporal forecasting of solar irradiation along a navigation route," *Appl. Energy*, vol. 211, pp. 15–27, Feb. 2018.
[46] S. Sun, L. Wei, J. Xu, and Z. Jin, "A new wind speed forecasting modeling strategy using two-stage decomposition, feature selection and DAWNN," *Energies*, vol. 12, no. 3, p. 334, Jan. 2019.
[47] T. Peng, J. Zhou, C. Zhang, and Y. Zheng, "Multi-step ahead wind speed forecasting using a hybrid model based on two-stage decomposition technique and AdaBoost-extreme learning machine," *Energy Convers. Manage.*, vol. 153, pp. 589–602, Dec. 2017.
[48] M. A. Colominas, G. Schlotthauer, and M. E. Torres, "Improved complete ensemble EMD: A suitable tool for biomedical signal processing," *Biomed. Signal Process. Control*, vol. 14, pp. 19–29, Nov. 2014.
[49] K. Dragomiretskiy and D. Zosso, "Variational mode decomposition," *IEEE Trans. Signal Process.*, vol. 62, no. 3, pp. 531–544, Nov. 2013.
[50] W. Li, Q. Shi, M. Sibtain, D. Li, and D. E. Mbanze, "A hybrid forecasting model for short-term power load based on sample entropy, two-phase decomposition and whale algorithm optimized support vector regression," *IEEE Access*, vol. 8, pp. 166907–166921, 2020.
[51] P. Yao, J. Xue, K. Zhou, and X. Wang, "Sample entropy-based approach to evaluate the stability of double-wire pulsed MIG welding," *Math. Problems Eng.*, vol. 2014, pp. 1–8, Jun. 2014.
[52] T. Liu, Z. Tan, C. Xu, H. Chen, and Z. Li, "Study on deep reinforcement learning techniques for building energy consumption forecasting," *Energy Buildings*, vol. 208, Feb. 2020, Art. no. 109675.
[53] D. R. Song, C. Yang, C. McGreavy, and Z. Li, "Recurrent deterministic policy gradient method for bipedal locomotion on rough terrain challenge," in *Proc. 15th Int. Conf. Control, Autom., Robot. Vis. (ICARCV)*, Nov. 2018, pp. 311–318.
[54] S. Hochreiter and J. Schmidhuber, "Long short-term memory," *Neural Comput.*, vol. 9, no. 8, pp. 1735–1780, 1997.
[55] H. Zang, L. Cheng, T. Ding, K. W. Cheung, M. Wang, Z. Wei, and G. Sun, "Application of functional deep belief network for estimating daily global solar radiation: A case study in China," *Energy*, vol. 191, Jan. 2020, Art. no. 116502.
[56] B. Brahma and R. Wadhvani, "Solar irradiance forecasting based on deep learning methodologies and multi-site data," *Symmetry*, vol. 12, no. 11, p. 1830, Nov. 2020.
[57] M. Lawrence, M. O'Connor, and B. Edmundson, "A field study of sales forecasting accuracy and processes," *Eur. J. Oper. Res.*, vol. 122, no. 1, pp. 151–160, Apr. 2000.
[58] F. S. Tabataba, P. Chakraborty, N. Ramakrishnan, S. Venkatramanan, J. Chen, B. Lewis, and M. Marathe, "A framework for evaluating epidemic forecasts," *BMC Infectious Diseases*, vol. 17, no. 1, p. 345, Dec. 2017.

[59] M. Majidpour, H. Nazaripouya, P. Chu, H. Pota, and R. Gadh, "Fast univariate time series prediction of solar power for real-time control of energy storage system," *Forecasting*, vol. 1, no. 1, pp. 107–120, Sep. 2018.

[60] J. E. Nash and J. V. Sutcliffe, "River flow forecasting through conceptual models part I—A discussion of principles," *J. Hydrol.*, vol. 10, no. 3, pp. 282–290, Apr. 1970.

[61] C. J. Willmott, S. M. Robeson, and K. Matsuura, "A refined index of model performance," *Int. J. Climatol.*, vol. 32, no. 13, pp. 2088–2094, Nov. 2012.

[62] S. Adnan, A. H. Khan, S. Haider, and R. Mahmood, "Solar energy potential in pakistan," *J. Renew. Sustain. Energy*, vol. 4, no. 3, May 2012, Art. no. 032701.

[63] Solargis. *Solar Resource Maps of Pakistan*. ESMAP-World Bank Group. [Online]. Available: https://solargis.com/maps-and-gis-data/download/pakistan

[64] World Bank. (2017). *Pakistan—Solar Radiation Measurement Data. World Bank via ENERGYDATA.Info, Under a Project Funded by the Energy Sector Management Assistance Program (ESMAP)*. Accessed: Jan. 2, 2020. [Online]. Available: https://datacatalog.worldbank.org/dataset/pakistan-solar-radiation-measurement-data

[65] M. Abadi, P. Barham, J. Chen, Z. Chen, A. Davis, J. Dean, M. Devin, S. Ghemawat, G. Irving, and M. Isard, "TensorFlow: A system for large-scale machine learning," in *Proc. 12th USENIX Symp. Operating Syst. Design Implement. (OSDI)*, 2016, pp. 265–283.

[66] A. Gulli and S. Pal, *Deep Learning With Keras*. Birmingham, U.K.: Packt, 2017.

[67] W. McKinney, "pandas: A foundational Python library for data analysis and statistics," *Python High Perform. Sci. Comput.*, vol. 14, no. 9, pp. 1–9, 2011.

[68] F. Pedregosa, G. Varoquaux, A. Gramfort, V. Michel, B. Thirion, O. Grisel, M. Blondel, P. Prettenhofer, R. Weiss, and V. Dubourg, "Scikit-learn: Machine learning in Python," *J. Mach. Learn. Res.*, vol. 12, pp. 2825–2830, Nov. 2011.

[69] S. van der Walt, S. C. Colbert, and G. Varoquaux, "The NumPy array: A structure for efficient numerical computation," *Comput. Sci. Eng.*, vol. 13, no. 2, pp. 22–30, Mar. 2011.

[70] J. D. Hunter, "Matplotlib: A 2D graphics environment," *Comput. Sci. Eng.*, vol. 9, no. 3, pp. 90–95, 2007.

[71] M. Waskom, O. Botvinnik, J. Ostblom, M. Gelbart, S. Lukauskas, P. Hobson, D. C. Gemperline, T. Augspurger, Y. Halchenko, and J. B. Cole. (2020). *Mwaskom/Seaborn: Version v0.10.1 (Apr. 2020)*. Zenodo. [Online]. Available: https://zenodo.org/record/3767070#.YD3DoRZRVPY, doi: 10.5281/zenodo.3767070.

[72] C. Voyant, M. Muselli, C. Paoli, and M.-L. Nivet, "Optimization of an artificial neural network dedicated to the multivariate forecasting of daily global radiation," *Energy*, vol. 36, no. 1, pp. 348–359, Jan. 2011.

[73] T. Wu, P. Zhou, K. Liu, Y. Yuan, X. Wang, H. Huang, and D. O. Wu, "Multi-agent deep reinforcement learning for urban traffic light control in vehicular networks," *IEEE Trans. Veh. Technol.*, vol. 69, no. 8, pp. 8243–8256, Aug. 2020.

[74] K. Mani, M. Kaushik, N. Singhania, and K. M. Krishna, "Learning adaptive driving behavior using recurrent deterministic policy gradients," in *Proc. IEEE Int. Conf. Robot. Biomimetics (ROBIO)*, Dec. 2019, pp. 2092–2098.

[75] Y. Liu, Q. Liu, H. Zhao, Z. Pan, and C. Liu, "Adaptive quantitative trading: An imitative deep reinforcement learning approach," in *Proc. AAAI Conf. Artif. Intell.*, Apr. 2020, vol. 34, no. 2, pp. 2128–2135.

[76] S. Fan, G. He, X. Zhou, and M. Cui, "Online optimization for networked distributed energy resources with time-coupling constraints," *IEEE Trans. Smart Grid*, vol. 12, no. 1, pp. 251–267, Jan. 2021.

[77] C. Enyioha, S. Magnússon, K. Heal, N. Li, C. Fischione, and V. Tarokh, "On variability of renewable energy and online power allocation," *IEEE Trans. Power Syst.*, vol. 33, no. 1, pp. 451–462, Jan. 2018.

[78] A. Bernstein and E. Dall'Anese, "Real-time feedback-based optimization of distribution grids: A unified approach," *IEEE Trans. Control Netw. Syst.*, vol. 6, no. 3, pp. 1197–1209, Sep. 2019.

[79] J. Li, Z. Xu, J. Zhao, and C. Zhang, "Distributed online voltage control in active distribution networks considering PV curtailment," *IEEE Trans. Ind. Informat.*, vol. 15, no. 10, pp. 5519–5530, Oct. 2019.

[80] C. Opathella, A. Elkasrawy, A. A. Mohamed, and B. Venkatesh, "Optimal scheduling of merchant-owned energy storage systems with multiple ancillary services," *IEEE Open Access J. Power Energy*, vol. 7, pp. 31–40, 2020.

[81] X. Liu, L. Che, K. Gao, and Z. Li, "Power system intra-interval operational security under false data injection attacks," *IEEE Trans. Ind. Informat.*, vol. 16, no. 8, pp. 4997–5008, Aug. 2020.

[82] M. G. Angle, S. Madnick, J. L. Kirtley, and S. Khan, "Identifying and anticipating cyberattacks that could cause physical damage to industrial control systems," *IEEE Power Energy Technol. Syst. J.*, vol. 6, no. 4, pp. 172–182, Dec. 2019.

[83] J. Tian, R. Tan, X. Guan, and T. Liu, "Enhanced hidden moving target defense in smart grids," *IEEE Trans. Smart Grid*, vol. 10, no. 2, pp. 2208–2223, Mar. 2019.

[84] M. Cui and J. Wang, "Deeply hidden moving-target-defense for cybersecure unbalanced distribution systems considering voltage stability," *IEEE Trans. Power Syst.*, early access, Oct. 15, 2020, doi: 10.1109/TPWRS.2020.3031256.

[85] C. Liu, J. Wu, C. Long, and D. Kundur, "Reactance perturbation for detecting and identifying FDI attacks in power system state estimation," *IEEE J. Sel. Topics Signal Process.*, vol. 12, no. 4, pp. 763–776, Aug. 2018.

[86] C. Chen, M. Cui, X. Fang, B. Ren, and Y. Chen, "Load altering attack-tolerant defense strategy for load frequency control system," *Appl. Energy*, vol. 280, Dec. 2020, Art. no. 116015.

MUHAMMAD SIBTAIN is currently pursuing the Ph.D. degree in electrical engineering with China Three Gorges University (CTGU). His research interests include forecasting and optimal management of renewable energy technologies for smart grids.



XIANSHAN LI received the Ph.D. degree in electrical engineering from China Three Gorges University. He is currently a Professor at China Three Gorges University. His main research interests include power system optimization, smart grid energy management, and operation optimization and control.

SNOOBER SALEEM is currently pursuing the master's degree in economics with the National University of Modern Languages (NUML). Her research interests include reinforcement learning and energy economics analysis.

QURAT-UL-AIN received the master's degree in business administration from the Hailey College of Banking and Finance (HCBF). Her research interests include deep learning applications for electricity markets.

MUHAMMAD SAQLAIN ASAD received the master's degree in electrical engineering. He is currently working as a Design Engineer in National Design and Engineering Solutions. His current research interests include deep learning approaches, clean energy systems design, integration, and forecasting.

TOUSEEF TAHIR received the master's degree in mechanical engineering. He is currently working as a Senior Engineer in Mangla Power Station. His research interests include power plant systems up-gradation and capacity enhancement, and optimal reservoir operation.



HALIT APAYDIN received the M.Sc. and Ph.D. degrees from the Ankara University Faculty of Agriculture, in 1995 and 2002, respectively. He is currently a Professor with the Ankara University Faculty of Agriculture. His main research interests include hydrology, water resources management, irrigation, geographic information systems, data mining, and artificial intelligence.